Article

Immunity

The Microglial Innate Immune Receptor TREM2 Is Required for Synapse Elimination and Normal Brain Connectivity

Graphical Abstract

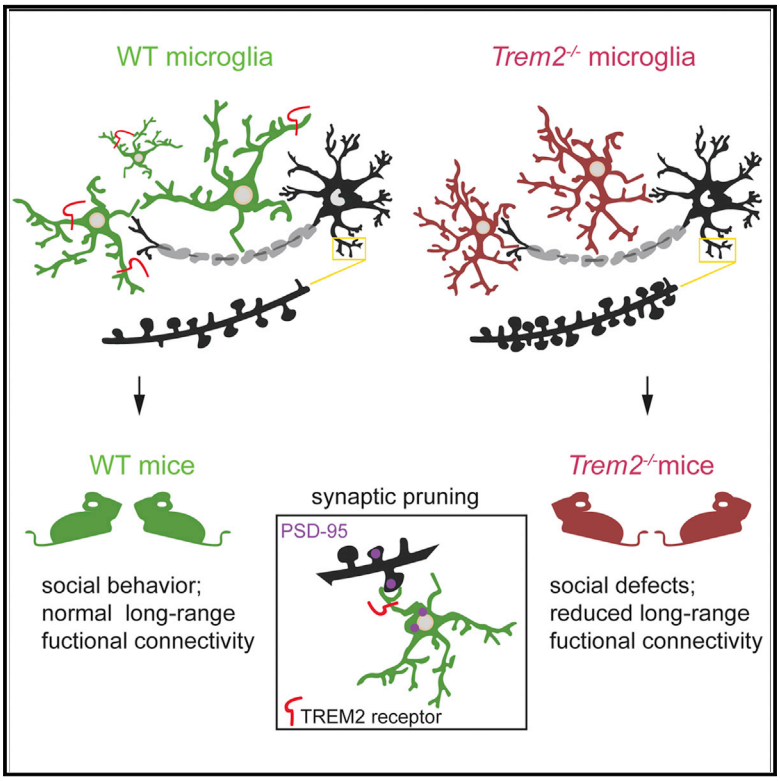

Authors

Fabia Filipello, Raffaella Morini, Irene Corradini, ..., Margaret Fahnestock, Rosa Chiara Paolicelli, Michela Matteoli

Correspondence

michela.matteoli@hunimed.eu

In Brief

TREM2 is a microglial innate immune receptor whose functions during brain development are still unknown. Filipello et al. demonstrate that TREM2 is essential for microglia to eliminate supernumerary synapses in the developing brain. TREM2 protein was also reduced in autistic patients, suggesting that the receptor may be involved in neurodevelopmental diseases.

Highlights

- Lack of TREM2 results in lower microglia activation during early brain development
- TREM2 is required for microglia-dependent synapse elimination
- Adult mice lacking TREM2 display sociability defects and altered brain connectivity
- TREM2 protein is reduced in patients affected by autism

Filipello et al., 2018, Immunity *48*, 979–991
May 15, 2018
https://doi.org/10.1016/j.immuni.2018.04.016

CellPress

Immunity
Article

The Microglial Innate Immune Receptor TREM2 Is Required for Synapse Elimination and Normal Brain Connectivity

Fabia Filipello,[1,10,11] Raffaella Morini,[2,10] Irene Corradini,[2,3] Valerio Zerbi,[4] Alice Canzi,[1] Bernadeta Michalski,[5] Marco Erreni,[6] Marija Markicevic,[4] Chiara Starvaggi-Cucuzza,[2] Karel Otero,[7] Laura Piccio,[8] Francesca Cignarella,[8] Fabio Perrucci,[2] Matteo Tamborini,[2] Marco Genua,[6] Lawrence Rajendran,[9] Elisabetta Menna,[2,3] Stefania Vetrano,[1] Margaret Fahnestock,[5] Rosa Chiara Paolicelli,[9] and Michela Matteoli[2,3,12,*]

[1]Humanitas University, Department of Biomedical Sciences, Via Rita Levi Montalcini, 20090 Pieve Emanuele – Milan, Italy
[2]Laboratory of Pharmacology and Brain Pathology, Humanitas Clinical and Research Center, Via Manzoni 56, 20089 Rozzano – Milan, Italy
[3]IN-CNR, 20129 Milano, Italy
[4]Neural Control of Movement Lab, HEST, ETH Zürich, Winterthurerstrasse 190, 8057 Zurich, Switzerland
[5]Department of Psychiatry & Behavioural Neurosciences, HSC-4N80, McMaster University, Hamilton, ON, Canada
[6]Department of Immunology and Inflammation, Humanitas Clinical and Research Center, Via Manzoni 56, 20089 Rozzano – Milan, Italy
[7]Department of Neuroimmunology, Acute Neurology and Pain, Biogen Inc., 115 Broadway, Cambridge, MA, USA
[8]Department of Neurology, Washington University, St. Louis, MO, USA
[9]Systems and Cell Biology of Neurodegeneration, IREM, University of Zurich, Schlieren, Switzerland
[10]These authors contributed equally
[11]Present address: Department of Neurology, Washington University, St. Louis, MO, USA
[12]Lead Contact
*Correspondence: michela.matteoli@hunimed.eu
https://doi.org/10.1016/j.immuni.2018.04.016

SUMMARY

The triggering receptor expressed on myeloid cells 2 (TREM2) is a microglial innate immune receptor associated with a lethal form of early, progressive dementia, Nasu-Hakola disease, and with an increased risk of Alzheimer's disease. Microglial defects in phagocytosis of toxic aggregates or apoptotic membranes were proposed to be at the origin of the pathological processes in the presence of *Trem2* inactivating mutations. Here, we show that TREM2 is essential for microglia-mediated synaptic refinement during the early stages of brain development. The absence of *Trem2* resulted in impaired synapse elimination, accompanied by enhanced excitatory neurotransmission and reduced long-range functional connectivity. *Trem2*$^{-/-}$ mice displayed repetitive behavior and altered sociability. TREM2 protein levels were also negatively correlated with the severity of symptoms in humans affected by autism. These data unveil the role of TREM2 in neuronal circuit sculpting and provide the evidence for the receptor's involvement in neurodevelopmental diseases.

INTRODUCTION

The triggering receptor expressed on myeloid cells 2 (TREM2) is an innate immune receptor of the immunoglobulin superfamily, expressed in different populations of myeloid cells including microglia in the central nervous system (CNS) (Kiialainen et al., 2005; Schmid et al., 2002). It consists of an extracellular V-type immunoglobin (Ig) domain, a transmembrane domain that associates with the adaptor protein TYRO protein tyrosine kinase-binding protein (TYROBP, also known as DAP12) and a cytoplasmic tail (Colonna, 2003; Peng et al., 2010; Wunderlich et al., 2013). TREM2 binds *in vitro* to anionic carbohydrates, bacterial products (LPS [lipopolysaccharides]), various phospholipids (Daws et al., 2003; Wang et al., 2015), and ApoE [apolipoprotein E]) (Atagi et al., 2015; Yeh et al., 2016). Initially identified as a phagocytic receptor for bacteria (N'Diaye et al., 2009), TREM2 is recognized to have anti-inflammatory properties on macrophages activated *in vitro* by Toll-like receptor (TLR) ligands (Hamerman et al., 2016; Turnbull et al., 2006).

TREM2 variants have been linked to different types of neurodegenerative disorders. Homozygous, loss-of-function mutations in *Trem2* or its signaling adapter DAP12 cause the autosomal recessive disorder Nasu–Hakola disease (Paloneva et al., 2002), a rare pathology characterized by early-onset dementia, demyelination, and bone cyst-like lesions. Rare variants in the *Trem2* gene appear as significant risk factors for late-onset Alzheimer's disease (AD) (Guerreiro et al., 2013; Jonsson et al., 2013), and a possible association has been proposed between TREM2 and Parkinson's disease, amyotrophic lateral sclerosis, and frontotemporal dementia (Cady et al., 2014; Kleinberger et al., 2017; Kober et al., 2016; Rayaprolu et al., 2013). TREM2 transduction pathways play a central role in promoting activation of microglia, which mostly express the receptor in the brain (Butovsky et al., 2014; Colonna, 2003). In a mouse model of AD, reduced TREM2 results in lower number of microglia surrounding plaques (Ulrich et al., 2014), reduced plaque compaction, and axonal dystrophy (Yuan et al., 2016). This has led to the hypothesis that the receptor plays a critical role in supporting microgliosis in response to pathological conditions in the CNS

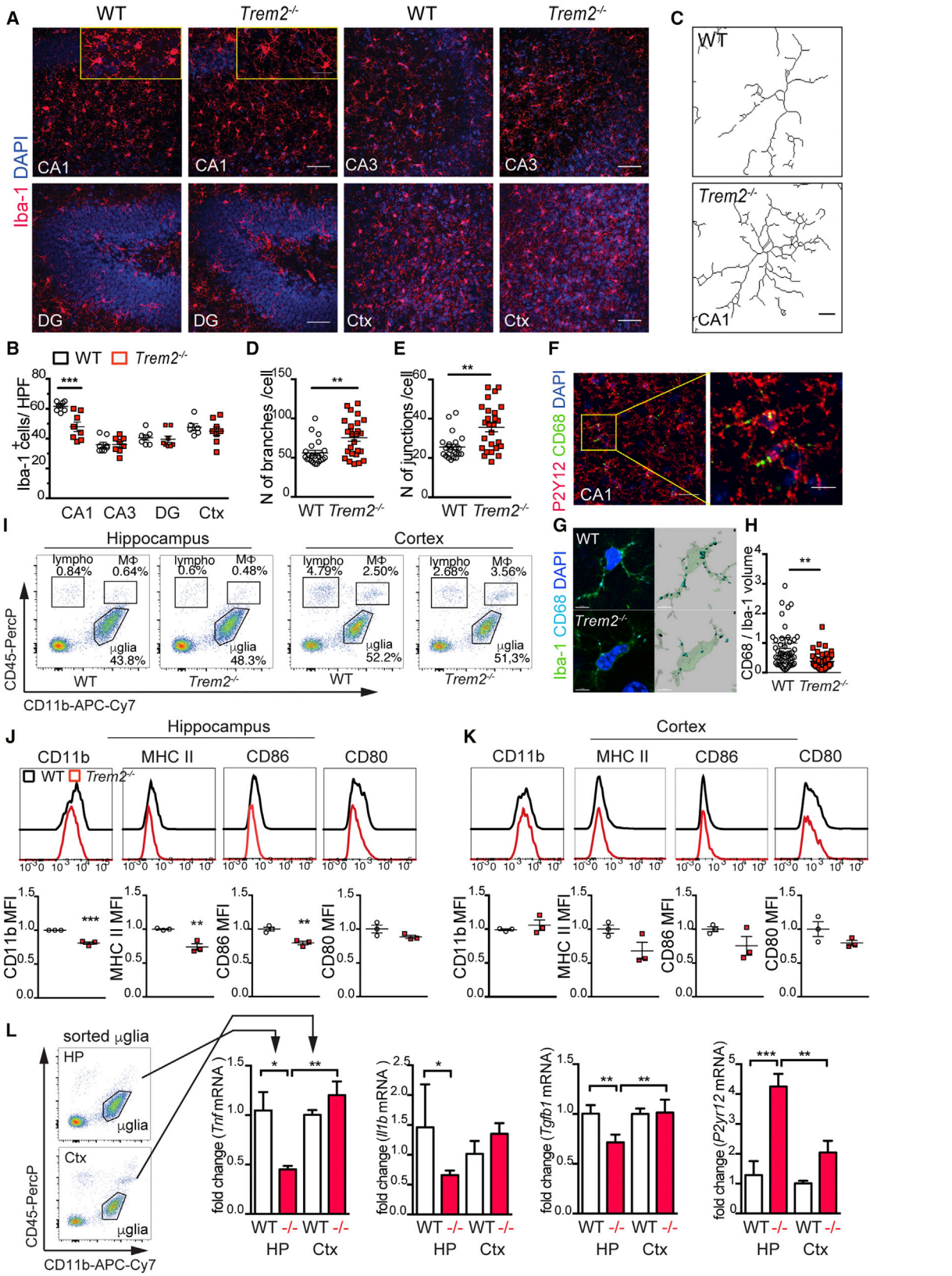

(legend on next page)

(Cantoni et al., 2015; Ransohoff and Cardona, 2010). On the other side, the activation of the TREM2-APOE pathway switches microglia towards a neurodegenerative phenotype (Krasemann et al., 2017), while the activation of a TREM2-dependent program contributes to generating a novel microglia type associated with neurodegenerative diseases (DAMs) (Keren-Shaul et al., 2017).

In recent years, microglia have emerged as critical players in the maturation of neural circuits during brain development, through the phagocytosis of supernumerary synapses via the fractalkine receptor CX3CR1 or complement receptor 3 (CR3 or CD11b) (Paolicelli et al., 2011; Schafer et al., 2012). Also, microglia control learning-dependent synaptic structural plasticity through brain-derived neurotrophic factor (BDNF) and tropomyosin receptor kinase B (TrkB) signaling pathways (Parkhurst et al., 2013) and, upon contact with somatosensory cortex dendrites, initiate filopodia formation during the intense spinogenesis occurring in the first two postnatal weeks (Miyamoto et al., 2016). Alterations in the process of synaptic pruning appear to be at the root of various neurodevelopmental diseases, including autism spectrum disorder (ASD) (Penzes et al., 2011).

Given the crucial role of microglia in the early phases of brain development, we investigated the possibility that TREM2 may regulate microglial activity at this critical time. Our results indicate that microglial TREM2 controls the process of supernumerary synapse elimination.

RESULTS

TREM2 Deficiency Affects Microglia Number and Activation during the Early Stages of Brain Development

TREM2 was selectively expressed by microglial cells in both the cortex and hippocampus of wild-type (WT) mice at different stages of neuronal development (Figures S1A and S1B). Staining for the myeloid cell marker ionized calcium-binding adapter molecule 1 (Iba-1) of brain sections from WT and *Trem2*$^{-/-}$ littermates at postnatal day (P)18–20, the time window of synaptic refinement, revealed a significant decrease in microglial cell density in the CA1 area of the hippocampus in *Trem2*$^{-/-}$ brains compared to WT, while no difference was detected in the CA3 region, dentate gyrus, and cortex (Figures 1A and 1B). Consistent results were obtained in brain sections from the same *Trem2*$^{-/-}$ mouse line generated by Dr. Colonna's lab and maintained at Washington University (Turnbull et al., 2006) (Figures S1C and S1D). The reduction of microglia number in the CA1 region of *Trem2*$^{-/-}$ mice was confirmed by staining for purinergic receptor P2Y12, which is exclusively expressed by microglia in the CNS (Hickman et al., 2013) (Figure S1E).

The analysis of cell morphology in the CA1 region of P18–20 *Trem2*$^{-/-}$ mice revealed a more ramified phenotype, with a higher number of branches and junctions per cell (Figures 1C–1E). Also, a decrease of the macrophage-specific lysosomal marker CD68 (Figures 1F and 1G) per Iba-1^{+} cell volume (Figure 1H) was detected in mutant mice, suggesting reduced activation of *Trem2*$^{-/-}$ microglia compared to WT. Consistently, fluorescence-activated cell sorting (FACS) analysis of P18–20 hippocampal and cortical Cd11b^{+}CD45^{low} microglia, positive for the ectonucleoside triphosphate diphosphohydrolase CD39 (Figure S1F) (Braun et al., 2000), revealed a decreased activation profile in *Trem2*$^{-/-}$ hippocampus, as indicated by the lower mean fluorescence intensity (MFI) of major histocompatibility complex class II (MHC-II), CD11b, and the B.7 costimulatory molecule CD86 (Figures 1I–1K).

Furthermore, and in line with previous results (Mazaheri et al., 2017), Cd11b^{+}CD45^{low} microglia sorted from *Trem2*$^{-/-}$ P18–20 mice and analyzed by quantitative real-time RT-PCR displayed reduced inflammatory molecules such as *Tnf*, *Tgfb1*, and *Il1b* genes and higher expression of the homoeostatic gene *P2ry12* (Butovsky et al., 2014) relative to WT (Figure 1L). Taken together, these data show that, in *Trem2*$^{-/-}$ mice, microglia are decreased in number and less activated specifically in the hippocampus.

Trem2$^{-/-}$ Mice Display Enhanced Excitatory Neurotransmission and Increased Synapse Density

To investigate whether mice lacking TREM2 develop neuronal defects, whole-cell recording of miniature excitatory postsynaptic currents (mEPSCs) was performed in pyramidal neurons of P18–20 acute brain slices. *Trem2*$^{-/-}$ neurons from the CA1 region displayed higher frequency of mEPSCs compared to WT, in the absence of changes in mEPSC amplitude (Figures 2A–2C). Consistent with mEPSC frequency increase reflecting a higher number of synaptic contacts, immunofluorescence analysis revealed higher density of the postsynaptic marker PSD95 (Figures 2D and 2F) and the presynaptic marker VGLUT1 (Figures 2E and 2G) in *Trem2*$^{-/-}$ compared to WT. Similar results were obtained with the presynaptic marker SV2A (WT mean = 0.99 ± SEM 0.27;

Figure 1. TREM2 Deficiency Affects Microglia Cell Density and Activation

(A) Microglia were counted as Iba-1^{+} cells per high-power field (HPF) in the CA1 and CA3 hippocampal (HP) regions, dentate gyrus (DG), and cortex (Ctx) in WT and *Trem2*$^{-/-}$ mice at P18–20. Original magnification, 40X. Scale bar, 50 μm. Zoomed-in inset images: scale bar, 25 μm.

(B) Quantification of microglia densities.

(C–E) Skeletonized reconstruction (C) and quantitative analysis of (D) total branches and (E) junctions per cell in the CA1. For microglia count, WT N = 4, n = 8 fields (CA1, CA3), n = 7 fields (DG), n = 6 fields (Ctx); *Trem2*$^{-/-}$ N = 6, n= 8 fields. ***p < 0.001, unpaired t test. For skeletonize analysis, WT N = 3, n = 23 fields; *Trem2*$^{-/-}$ N = 3, n = 26 fields. **p < 0.01, Mann Whitney test. Scale bar, 25 μm. Original magnification, 40X.

(F) Confocal images of CD68^{+} structures within P2Y12^{+} microglia in P18–20 WT mice. Scale bar, 25 μm.

(G and H) 3D reconstruction (G) and relative quantification (H) of CD68^{+} structures per Iba-1 volume. Scale bar, 5 μm. WT N = 5, n = 51 cells; *Trem2*$^{-/-}$ N = 8, n = 52 cells. **p < 0.01, unpaired t test.

(I) Microglia were identified as CD11b^{+}CD45^{low} cells upon doublet discrimination and death cell exclusion. Values indicated in FACS plots have to be considered as the relative frequency on the total single live cells.

(J and K) Histograms (J) showing MFIs of surface MHC-II, CD80, CD86, and CD11b and (K) relative quantification. **p < 0.01, ***p < 0.001, unpaired t test. WT N = 3 and *Trem2*$^{-/-}$ N = 3.

(L) Relative mRNA expression by qRT-PCR of microglia cells sorted from the HP and Ctx of P18–20 WT and *Trem2*$^{-/-}$ mice. WT N = 2 and *Trem2*$^{-/-}$ N = 2. *p < 0.05, **p < 0.01, ***p < 0.001. One-way ANOVA followed by Tukey's multiple comparisons test. See also Figure S1.

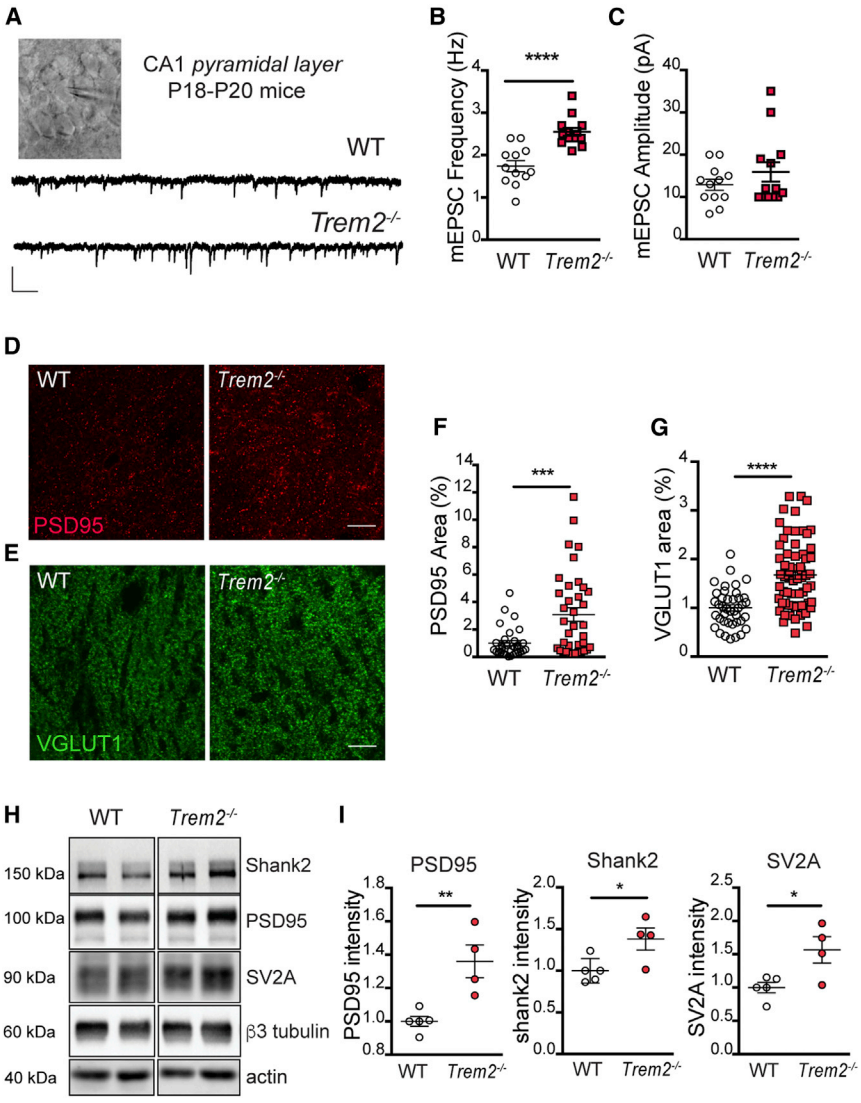

Figure 2. Neuronal Activity and Synaptic Marker Expression Is Increased in *Trem2*$^{-/-}$ Mice

(A) Representative traces of mEPSC recordings in CA1 hippocampal acute slices from *Trem2*$^{-/-}$ and WT mice.

(B and C) Summary graph of mEPSC frequency (B) and amplitude (C). mEPSC frequency: WT 1.739 ± 0.131, N = 5, n = 12 cells; *Trem2*$^{-/-}$ 2.550 ± 0.09, N = 5, n = 13 cells. mEPSC amplitude: WT 12.8 ± 2; *Trem2*$^{-/-}$ 14.5 ± 3. ****p < 0.0001, unpaired t test. Scale bars, 10 pA, 250 ms.

(D–G) Representative fields (D and E) and relative quantification (F and G) of the CA1 region of P18–20 mice, stained for PSD95 (D and F) and for VGLUT1 (E and G). Scale bar, 10μm. (F) WT N = 5, n = 32 fields; *Trem2*$^{-/-}$ N = 5, n = 37 fields. (G) WT N = 6, n = 40 fields; *Trem2*$^{-/-}$ N = 5, n = 65 fields. ***p < 0.001, ****p < 0.0001, unpaired t test.

(H and I) Western blot analysis (H) and quantification (I) of PSD95, Shank2, and SV2A in the whole hippocampus of P18–20 mice. WT N = 4 and *Trem2*$^{-/-}$ N = 5. *p < 0.05, **p < 0.005, unpaired t test. See also Figure S1.

Trem2$^{-/-}$ mean = 2.46 ± SEM 0.26 area%). Increased expression of PSD95, Shank2, and SV2A was detected by western blotting of *Trem2*$^{-/-}$ hippocampal homogenates (Figures 2H and 2I). No differences in the number or stratification of CA1 neurons in *Trem2*$^{-/-}$ versus WT mice were detected by Nissl staining (Figure S1G) or by NeuN^{+} cell counting (Figure S1H). Also, no difference was detected in the expression of the dendritic marker MAP2 (Figure S1I), further supporting the increase of synaptic sites, rather than increased neuronal branching, in *Trem2*$^{-/-}$ neurons. These results indicate enhanced pre- and postsynaptic contacts and increased electrophysiological activity in the absence of functional TREM2.

Microglial TREM2 Promotes Spine Elimination *In Vitro*

We next investigated whether the enhanced excitatory neurotransmission in brain slices could be determined by a neuron-autonomous defect. Patch-clamp recording of primary cultures of hippocampal neurons from WT or *Trem2*$^{-/-}$ postnatal mice (P0–1) revealed comparable mEPSC frequency and amplitude between *Trem2*$^{-/-}$ and WT neurons (Figures 3A and 3B), indicating that lack of TREM2 does not directly affect neuronal properties.

Since TREM2 is mostly expressed by microglia (Butovsky et al., 2014; Colonna, 2003) and we demonstrated that these cells display a defective profile in *Trem2*$^{-/-}$ mice (Figure 1), we hypothesized that the synaptic defects observed in the absence of TREM2 could be ascribed to a specific microglial dysfunction. We therefore analyzed the functional properties of microglia isolated from *Trem2*$^{-/-}$ and WT pups. No differences in the survival rate of WT versus *Trem2*$^{-/-}$ microglia were detected by Hoechst and propidium iodide staining 48 hr after cell plating, indicating comparable cell viability (Figure S2A). However, and in line with previous literature reporting that *Trem2*$^{-/-}$ microglia are unable to efficiently phagocytose apoptotic neuronal membranes (Neumann and Takahashi, 2007; Takahashi et al., 2005), we confirmed, by FACS quantitation, that *Trem2*$^{-/-}$ primary microglia phagocytosed significantly fewer apoptotic membranes than WT microglia (Figure S2B), despite being equally efficient at phagocytosing beads (Figure S2C). These observations led us to hypothesize that TREM2 regulates microglia phagocytic capacity during the period of synapse elimination, which corresponds to the developmental window where *Trem2*$^{-/-}$ microglia displayed an altered profile (Figure 1). To address this possibility, we co-cultured WT or *Trem2*$^{-/-}$ microglial cells in contact with WT hippocampal neurons (Figure 3C). Consistent with the ability of microglia to phagocytose synapses (Ji et al., 2013; Lui et al., 2016), culturing neurons for 24 hr with WT microglia resulted in synapse elimination, as indicated by the reduction of both mEPSC frequency (Figures 3D and 3E) and mushroom spine density (Figures 3F–3I). Microglia lacking TREM2 failed to

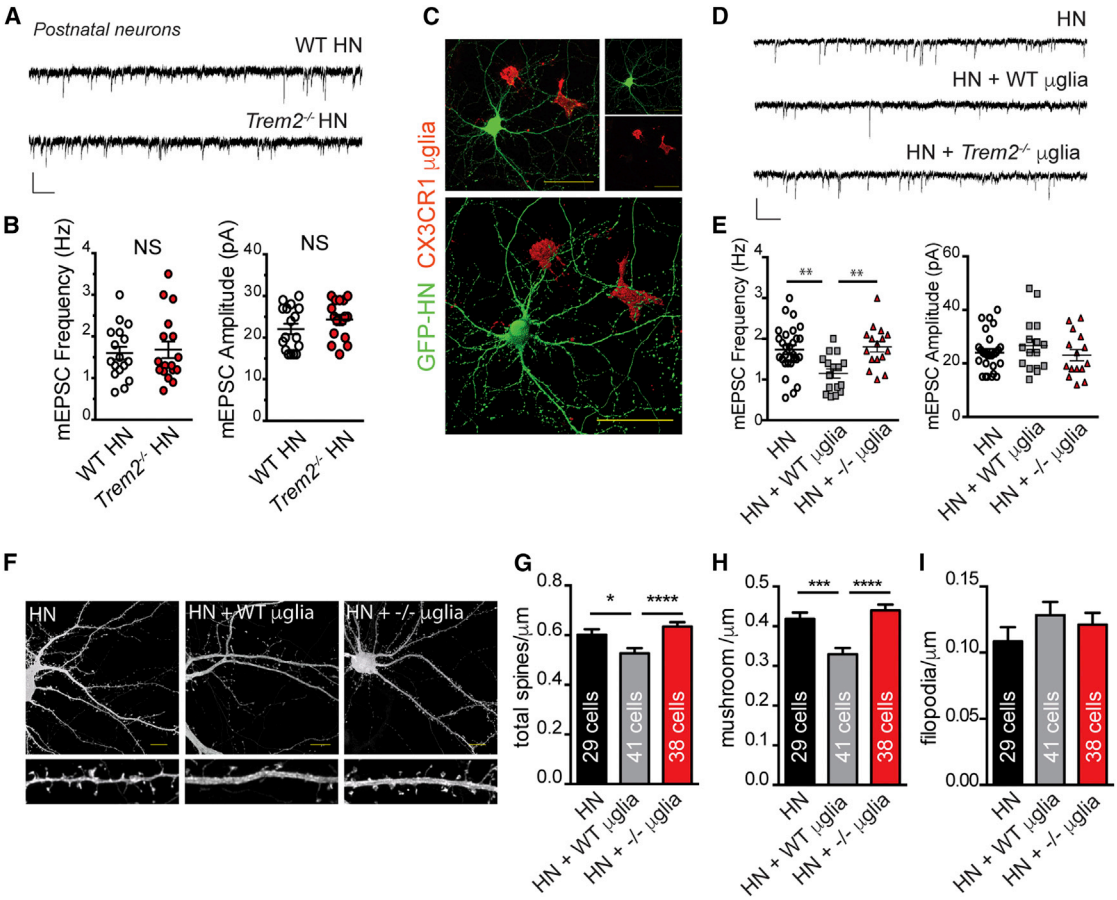

Figure 3. TREM2 Is Required by Microglial Cells to Perform Spine Refinement

(A and B) Representative traces of mEPSCs recorded from WT and *Trem2*$^{-/-}$ postnatal hippocampal neurons *in vitro* (HNs) (A) and quantification (B). mEPSC frequency: WT 1.639 ± 0.17, n = 15 cells; *Trem2*$^{-/-}$ 1.731 ± 0.22, n = 15 cells. mEPSC amplitude: WT 21.8 ± 1.3; *Trem2*$^{-/-}$ 23.9 ± 1.16.

(C) Confocal images and 3D reconstruction of CX3CR1^{+} microglia cells (red) and GFP-transfected neurons (green) co-cultures. Scale bar, 30 μm.

(D and E) Representative traces (D) and quantitation (E) of mEPSC recordings in WT HNs cultured alone or co-cultured with either WT or *Trem2*$^{-/-}$ microglia for 24 hr. mEPSs frequency: HN 1.733 ± 0.10, n = 28 cells; HN + WT microglia 1.149 ± 0.10, n = 16 cells; HN + *Trem2*$^{-/-}$ microglia 1.803 ± 0.12, n = 16 cells. mEPSC amplitude: HN 24 ± 1.2; HN + WT microglia 26.5 ± 2; HN + *Trem2*$^{-/-}$ microglia 23 ± 2; **p < 0.01. One-way ANOVA followed by Tukey's multiple comparisons test. Scale bars, 10 pA and 250 ms.

(F) HNs cultured alone or co-cultured with either WT or *Trem2*$^{-/-}$ microglia. Scale bar, 10 μm.

(G–I) Analysis of total spine (G), mushroom spine (H), and filopodia (I) density under the conditions described above. Number of total spines/μm, HN 0.6 ± 0.02, dendrites: 63, neurons: 29; HN + WT microglia 0.52 ± 0.02, dendrites: 101, neurons: 41; HN + *Trem2*$^{-/-}$ microglia 0.63 ± 0.16, dendrites: 94, neurons: 38. Number of mushroom spines/μm, HN 0.41 ± 0.01; HN + WT microglia 0.32 ± 0.01; HN + *Trem2*$^{-/-}$ microglia 0.43 ± 0.01. Number of filopodia/μm, HN 0.10 ± 0.01; HN + WT microglia 0.12 ± 0.01; HN + *Trem2*$^{-/-}$ microglia 0.12. *p < 0.05, ***p < 0.001, ****p < 0.0001. One-way ANOVA followed by Dunn's multiple comparison test. Bar graphs represent mean ± SEM of 4 independent experiments. See also Figure S2.

remove spines (Figures 3F–3H) or to reduce mEPSC frequency (Figure 3E) when added to neuronal cultures, indicating lack of synapse elimination. Preventing contact between microglia and neurons, by the use of transwell inserts, did not result in reduced mEPSC frequency or spine density, neither in the presence of WT nor *Trem2*$^{-/-}$ microglia (Figures S2D–S2F). These data demonstrate that microglial TREM2 is required for mediating synapse elimination through a process requiring cell-to-cell contact.

TREM2 Is Required for Synapse Engulfment *In Vivo*

To further assess whether lack of TREM2 impairs phagocytosis of synaptic structures, primary microglia were cultured in the presence of synaptosomes labeled with FM1-43 fluorescent dye. Figure 4A shows Iba-1^{+} microglial cells displaying colocalization between FM1-43^{+} synaptosomes and CD68^{+} phagolysosomal structures. Measurement of engulfment capacity by FACS revealed that *Trem2*$^{-/-}$ microglia display significantly reduced engulfment of synaptosomes compared to their WT counterparts (Figures 4B–4D).

To investigate whether *Trem2*$^{-/-}$ microglia were defective in the synapse elimination also *in vivo*, the amount of PSD95 within microglial phagolysosomes was analyzed by immunofluorescence in hippocampal sections from P18–20 *Trem2*$^{-/-}$ or WT brains. Significantly lower PSD95 puncta were detectable in CD68^{+} structures of *Trem2*$^{-/-}$ microglia than in those of WT (Figures 4E and 4F), paralleled by a higher amount of total PSD95 per field (Figure 4G). These results were faithfully replicated in

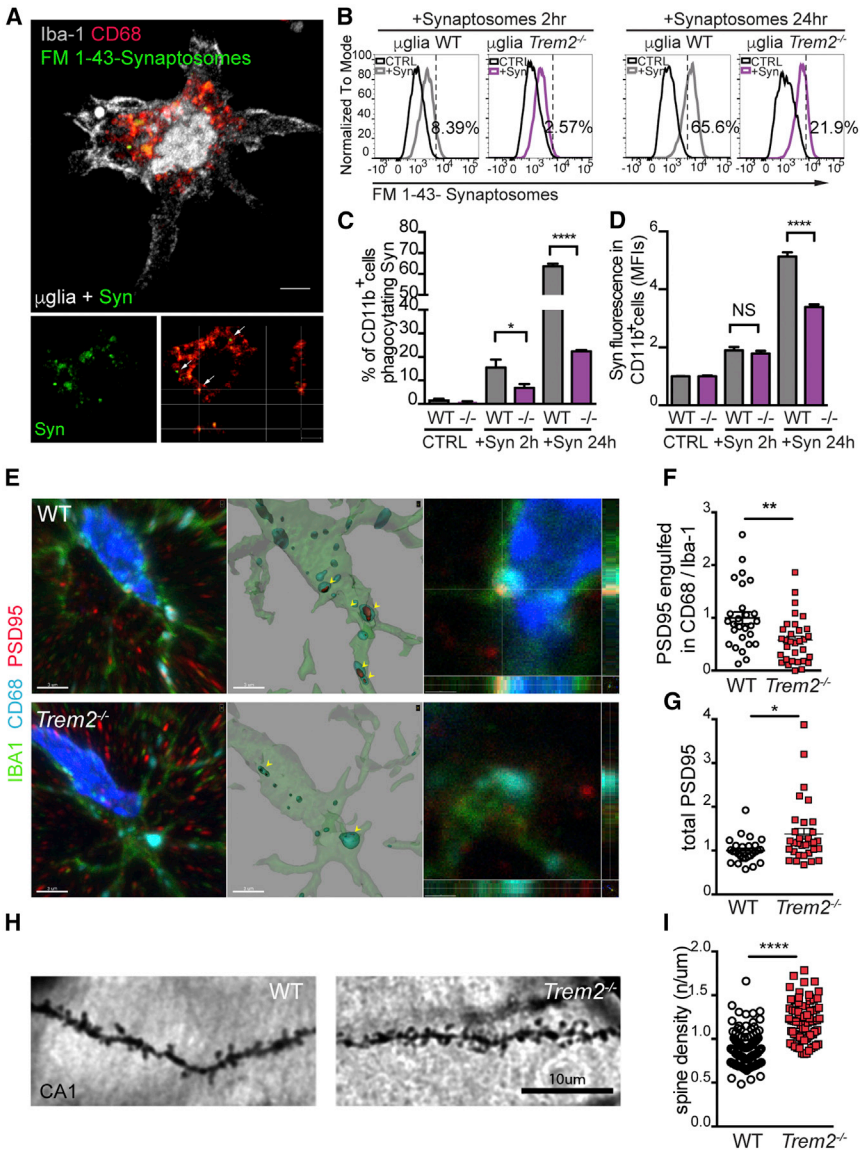

Figure 4. TREM2 Is Required for Synapse Engulfment

(A) Confocal and orthogonal images of FM1-43 dye-labeled synaptosomes (Syns) colocalizing with CD68$^+$ structures (white arrows) inside microglia *in vitro*. Scale bar, 5 µm.

(B) Representative FACS profiles of WT or *Trem2*$^{-/-}$ CD11b$^+$ microglia populations for FM1-43 dye intensity after the incubation with FM1-43-conjugated Syns for 2 or 24 hr.

(C–D) Engulfment ability of *Trem2*$^{-/-}$ and WT microglia, calculated by comparing the percentage (C) or the MFIs (D) of CD11b$^+$ cells expressing strong FM1-43 dye intensity. Bar graphs represent mean ± SEM of 3 independent experiments. *p < 0.05, ****p < 0.0001. One-way ANOVA followed by Tukey's multiple comparison test.

(E) Representative confocal z stack and relative 3D surface rendering showing volume reconstruction of microglia, CD68 and engulfed PSD95, detected within microglial CD68$^+$ structures (yellow arrowheads). On the right, orthogonal view of CD68$^+$ phagolysosomes colocalizing with PSD95. Scale bar, 3 µm.

(F and G) Relative quantification of engulfed PSD95 within CD68 per microglia (F) and total volume of PSD95$^+$ puncta per stack (G). WT N = 5, n = 27; *Trem2*$^{-/-}$ N = 6, n = 32.

(H and I) Representative images (H) of secondary branches of apical dendrites of WT and *Trem2*$^{-/-}$ CA1 neurons (P18–20) stained by the Golgi-Cox method and (I) relative quantitation. Number of spines/µm: WT 0.89 ± 0.01, N = 3, n = 110 dendrites; *Trem2*$^{-/-}$ 1.2 ± 0.02, N = 3, n = 77 dendrites. ****p < 0.0001, unpaired t test. Scale bar, 10 µm. See also Figure S2.

Trem2$^{-/-}$ mice from the Washington University colony (Figures S2G and S2H).

As a final confirmation of defective spine elimination *in vivo*, Golgi staining of CA1 pyramidal neurons revealed a significantly higher spine density in *Trem2*$^{-/-}$ mice (Figures 4H and 4I). These data, consistent with the higher content of synaptic markers (Figure 2), show a key role of the TREM2 in synapse elimination during brain development.

Trem2$^{-/-}$ Mice Display an Underconnectivity Phenotype between Prefrontal and Hippocampal Regions

Since reduction in synaptic pruning during development has been associated with reduced functional brain connectivity using resting-state fMRI (rs-fMRI) (Zhan et al., 2014), we aimed to assess whether the defective synaptic engulfment occurring in *Trem2*$^{-/-}$ mice during development results in altered connectivity in adulthood. To probe the existence of aberrant functional connections in 3-month-old (P90) *Trem2*$^{-/-}$ mice, the blood-oxygen-level-dependent (BOLD) time series were extracted from 130 bilateral regions of interest (ROIs) using the Allen Reference Atlas ontology (Sethi et al., 2017), and their connectivity couplings were measured using regularized Pearson's correlation coefficients (Grandjean et al., 2017). Only macro-areas that were fully covered by the field of view used for rs-fMRI acquisition were included in the analysis (isocortex, hippocampal formation, cortical subplate, striatum, pallidum, and thalamus) (Figure 5A). Uncorrected permutation testing (5,000 permutations) revealed an overall underconnectivity phenotype of *Trem2*$^{-/-}$ mice when compared to their WT littermates (Figure 5B). Multiple comparisons correction using network-based statistics (NBS) (Zalesky et al., 2010) identified a single, symmetric network with reduced connectivity (p = 0.011), which comprises 20 nodes (i.e., ROIs) and 68 edges (i.e., connections) as depicted in Figures 5C and 5D. The strongest differences were seen in connectivity between retrosplenial cortices (RSPs), subiculum (SUB), hippocampus (CA1 and DG), and anterior cingulate (ACA) (Figure 5E).

The structural integrity of major axon bundles was quantified by extracting fractional anisotropy (FA) values from seven white matter structures identified by the Allen Mouse Brain atlas.

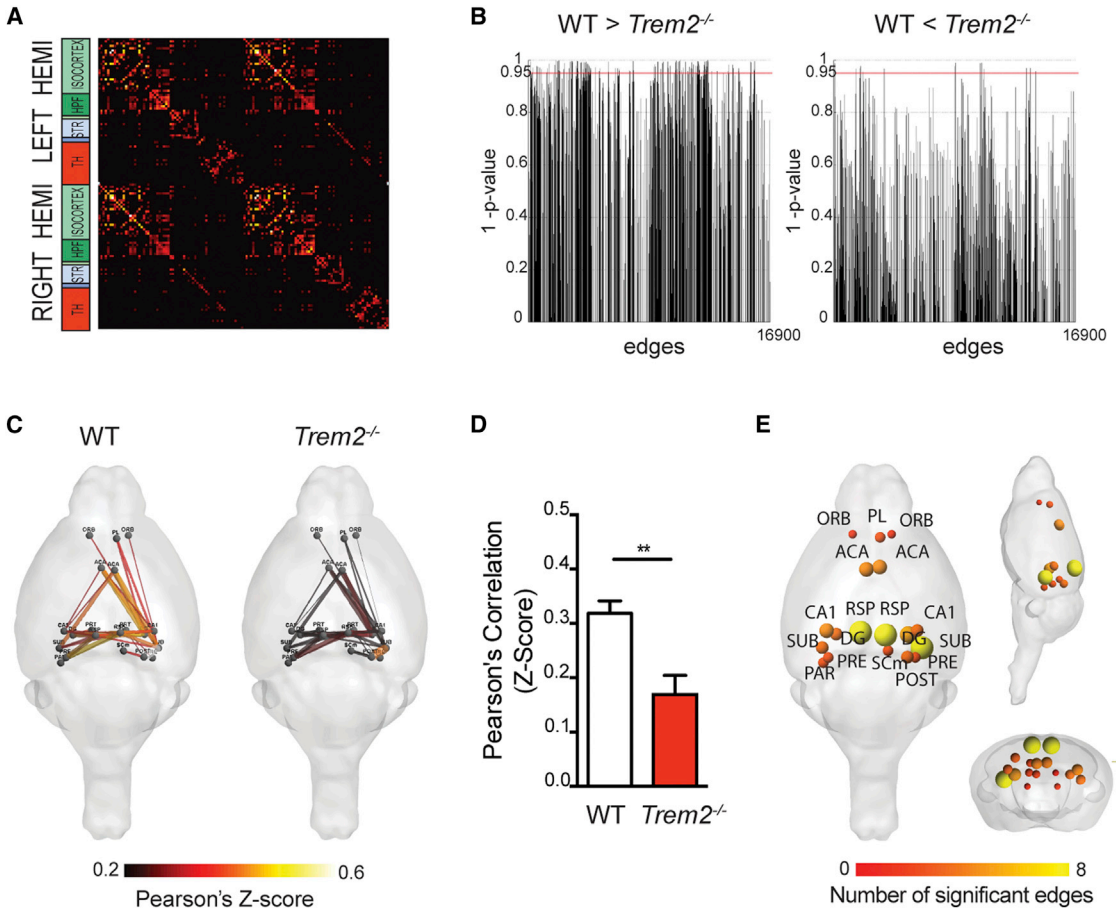

Figure 5. Decreased fMRI Functional Connectivity in *Trem2*$^{-/-}$ Mice

(A) Matrix representation of the whole-brain functional connectome (130 x 130 nodes, 10% sparsity) in the mouse brain, obtained from the average of 20 datasets.

(B) Results of group-difference permutation testing (5,000 permutations, uncorrected) are shown for two contrasts (WT > *Trem2*$^{-/-}$ and WT < *Trem2*$^{-/-}$).

(C) Correction for multiple comparisons using NBS revealed one significant large-scale network (p = 0.011, corrected) that includes connections between prefrontal cortical areas (anterior cingulate, ACA; orbitofrontal, ORB; prelimbic [PL] and retrosplenial [RSP] with hippocampal areas [CA1, DG] and subiculum [SUB; presubiculum, PRE, postsubiculum, POST]).

(D) For this network, a significant reduction in connectivity was found in *Trem2*$^{-/-}$ mice.

(E) Nodes of the circuit are represented as spheres, with size and color proportional to the numbers of significant under-connected edges. WT N = 9; *Trem2*$^{-/-}$ N = 10. **p < 0.01, unpaired t test. See also Figure S3 and Table S3.

All white matter tracts did not exhibit genotype differences between *Trem2*$^{-/-}$ mice and WT littermates (Figures S3A and Table S3). Taken together, these data suggest that the absence of TREM2 does not compromise the anatomical connections between brain regions but rather impairs their function.

Of note, Golgi staining and immunohistochemical analysis of P90 mice supported the occurrence of defective synaptic growth in the CA1 region of adult *Trem2*$^{-/-}$ mice. Indeed, different from WT mice, which displayed a relevant increase in spine density between P20 and P90, no spine augmentation occurred in *Trem2*$^{-/-}$ mice within the same developmental window (Figure S3B). In line with defective synaptic growth in *Trem2*$^{-/-}$ hippocampus, a lower amount of PSD95 protein was detectable in P90 *Trem2*$^{-/-}$ than in P20 *Trem2*$^{-/-}$ hippocampi (Figure S3C). Notably, both density and morphology of microglia cells were recovered to normal in P90 *Trem2*$^{-/-}$ mice (Figures S3D and S3E), in line with literature showing lack of differences in microglia of adult WT and *Trem2*$^{-/-}$ mice (Poliani et al., 2015). These data indicate that *Trem2*$^{-/-}$ mice display defects in brain circuit formation.

Trem2$^{-/-}$ Mice Display Altered Behavioral Phenotype

We next investigated whether adult (P90) *Trem2*$^{-/-}$ mice display altered behavioral performances. P90 *Trem2*$^{-/-}$ mice buried a significantly lower number of marbles relative to their WT littermates (Figures 6A and 6B) in the marble burying task and displayed a strong increase in self-grooming behavior (Figure 6C), traits typically altered in mouse models of ASD (Greco et al., 2013; Kim et al., 2016). Conversely, no alterations were observed in nestlet shredding (Figure 6D). *Trem2*$^{-/-}$ mice were defective also in social behavior. Indeed, differently from WT mice, which spent a longer time exploring the chamber with the stranger mouse than the empty compartment, *Trem2*$^{-/-}$ mice spent a comparable amount of time in the two chambers (Figure 6E). No defects were detected in the social recognition task, where *Trem2*$^{-/-}$ mice performed similarly to controls (Figure 6F). Social

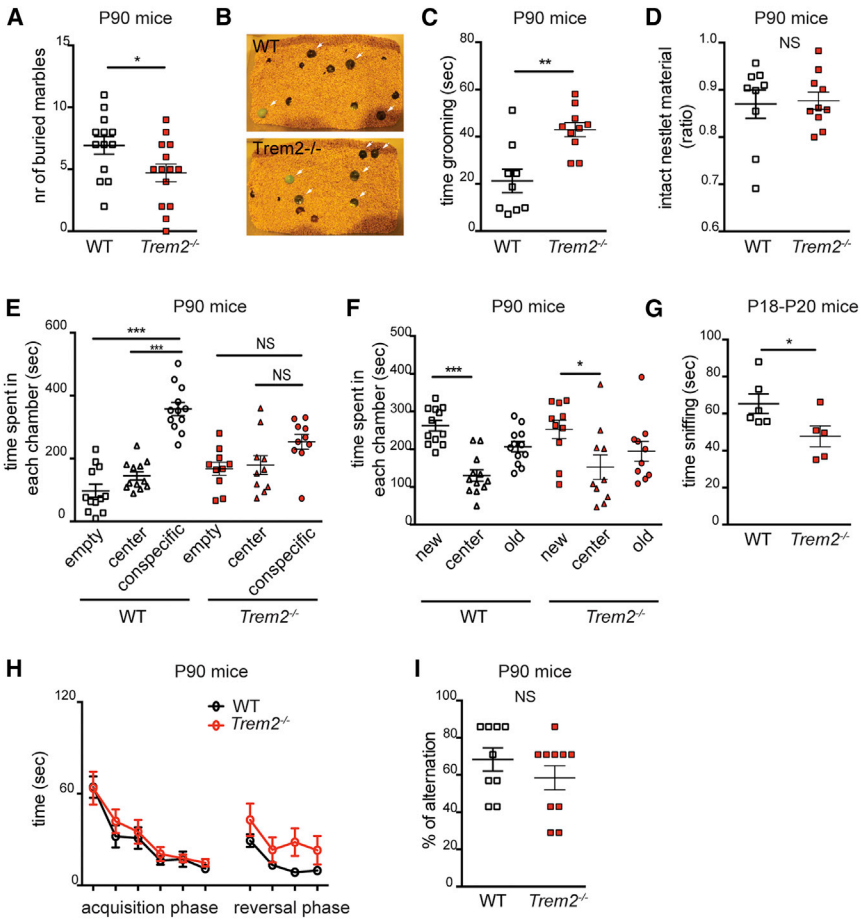

Figure 6. P90 *Trem2*$^{-/-}$ Mice Display Impairments in Repetitive and Social Behaviors

(A–F) P90 mice.

(A and B) Marble burying task: number of buried marbles during 30 min (A) and representative pictures (B) (white arrows indicate not-buried marbles). *p < 0.05, unpaired t test. WT N = 13; *Trem2*$^{-/-}$ N = 14.

(C) Self-grooming test. **p < 0.01, unpaired t test. WT N = 9; *Trem2*$^{-/-}$ N = 10.

(D) Percentage of intact material in nestlet shredding. WT N = 9; *Trem2*$^{-/-}$ N = 10.

(E) Sociability test performed in a social choice paradigm. ***p < 0.001. One-way ANOVA followed by Tukey's multiple comparison test. WT N = 12; *Trem2*$^{-/-}$ N = 10.

(F) Social memory test performed in a social novelty paradigm. *p < 0.05, ***p < 0.001. One-way ANOVA followed by Tukey's multiple comparison test. WT N = 12; *Trem2*$^{-/-}$ N = 10.

(G) P18–20 mice. Juvenile play interaction assessed as time of reciprocal sniffing. *p < 0.05, unpaired t test. WT 6 pairs (N = 12); *Trem2*$^{-/-}$ 5 pairs (N = 10).

(H and I) P90 mice. (H) Morris water maze place navigation task. Each point represents 3 trials. WT N = 22; *Trem2*$^{-/-}$ N = 16. (I) Spontaneous alternation in the T maze. WT N = 9; *Trem2*$^{-/-}$ N = 10. See also Figure S4.

defects were also detectable as early as P18–20, when a reduction of reciprocal sniffing time during juvenile play was found in *Trem2*$^{-/-}$ mice compared to WT (Figure 6G).

Consistent with the lack of impairment in social memory, P90 *Trem2*$^{-/-}$ mice did not display defects in the acquisition phase or in reversal learning in the Morris water maze (Figure 6H). Also, in the alternating T-maze working memory task (Deacon and Rawlins, 2006), *Trem2*$^{-/-}$ mice performed similarly to WT (Figure 6I).

General locomotor activity, as assessed by an automated open-field system, was not significantly altered in *Trem2*$^{-/-}$ versus WT mice, as indicated by comparable distance traveled, ambulatory counts, resting time, and zone entries, although a slight but significant increase was observed in average velocity over 30 min (Figures S4B–S4D, S4G, and S4H). Environment exploration was not affected in P90 *Trem2*$^{-/-}$ mice (Figure S4A). Also, no differences were observed in anxiety-related motor paradigms, as shown by comparable time spent in the corners of the arena or close to the walls (Figures S4E and S4F).

General motor activity of *Trem2*$^{-/-}$ mice, examined at P18–20, revealed lack of alterations in *Trem2*$^{-/-}$ mice relative to WT mice of the same age (Figures S4I–S4K). Also, P18–20 *Trem2*$^{-/-}$ mice did not display variations in anxiety-related activity, as shown by a similar time spent in the corners or close to the wall of the arena compared to WT mice (Figures S4L and S4M).

These data indicate that lack of TREM2 expression during development leads to behavioral defects reminiscent of ASD.

TREM2 Protein Negatively Correlates with Severity of Autism Symptoms

Given that defective synaptic pruning and dysfunctional microglia are associated with ASD (Tang et al., 2014) and that connectome analysis and behavioral phenotyping of *Trem2*$^{-/-}$ mice were reminiscent of ASD, we examined TREM2 protein levels in post-mortem brains of patients affected by idiopathic autism. Patients included in the age window between 5 and 23 years (i.e., the developmental period coinciding with synaptic pruning in humans; Stiles and Jernigan, 2010) displayed a significant reduction of TREM2 protein expression relative to healthy subjects (Figures 7A and 7B). Furthermore, an inverse correlation was found between the TREM2 protein levels and the Autism Diagnostic Interview-Revised (ADI-R) score (Lord et al., 1994) measured in ASD patients (Figure 7A and Table S3). Overall, these data highlight a critical role of TREM2 in ASD in humans.

DISCUSSION

Microglial phagocytosis relies on cell surface receptors, coupled to downstream signaling pathways that control actin remodeling and particle engulfment. TREM2 is one of these receptors that control the phagocytosis of apoptotic cell debris and reduces secretion of pro-inflammatory factors (Hsieh et al., 2009; Takahashi et al., 2005; Turnbull et al., 2006). Due to its phagocytic function, TREM2 is thought to be protective, and indeed, inactivating mutations in *Trem2* gene have been associated with different neurodegenerative diseases (Yeh et al., 2017).

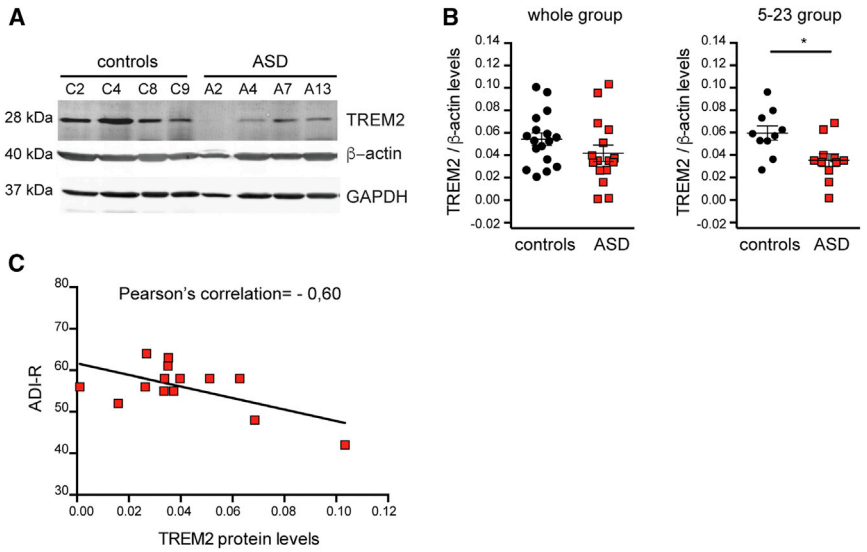

Figure 7. TREM2 Protein Is Decreased in 5- to 23-Year-Old Autistic Patients

(A) Representative western blot of fusiform gyrus samples from autistic patients and controls probed with TREM2, β-actin, and GAPDH (glyceraldehyde 3-phosphate dehydrogenase) antibodies.

(B) Quantification of TREM2 levels normalized to β-actin in controls (black circles) and patients (red squares) for the whole group (controls n = 17; ASD patients n = 16) (left) or for subjects included in the age window between 5 and 23 years (controls n = 10, ASD patients n = 11) (right). Unpaired t test: for the whole group, p = 0.1798; for the 5–23 age group, *p < 0.05 (p = 0.0101).

(C) Correlation between ADI-R and TREM2 protein levels. Pearson's correlation = −0.60, significance (two-tailed) *p = 0.023. ADI-R scores were available for 14 of the 16 ASD patients (red squares). See also Figure S5 and Tables S1, S2, and S4.

Our study unveils a role for TREM2 in the control of the microglia-dependent pruning of supernumerary synapses in the developing brain. The process of synaptic pruning is central during brain development, when the excess number of synaptic contacts is subsequently eliminated. Correct synaptic pruning is necessary for the strengthening of remaining synapses and is critical for normal brain development (Riccomagno and Kolodkin, 2015). Microglial cells play major roles in the process of synaptic pruning, participating in synapse remodeling and plasticity (Kettenmann et al., 2013; Paolicelli et al., 2011; Schafer et al., 2012; Tremblay et al., 2010).

The defective synapse elimination detected in *Trem2*$^{-/-}$ mice is paralleled by a reduction in the number of microglia in the hippocampus. This is in line with the finding that microglia lacking TREM2 migrate less efficiently towards apoptotic neurons *in vivo* (Mazaheri et al., 2017), a feature that we have observed also in our model using a scratch test (Figure S5A). Although we cannot exclude that defective migration of *Trem2*$^{-/-}$ microglia to the hippocampus may contribute to the observed defect in hippocampal synapse elimination, the finding that *Trem2*$^{-/-}$ microglia in the hippocampus display reduced internalization of synaptic markers inside CD68^{+} phagolysosomal structures, together with the evidence of defective synapse elimination when neurons and *Trem2*$^{-/-}$ microglia are cultured in contact, points to TREM2 being involved in synapse phagocytosis. Consistently, a higher density of presynaptic structures and dendritic spines was visible in the hippocampi of P18–20 *Trem2*$^{-/-}$ mice, paralleled by enhanced excitatory neurotransmission in acute brain slices. The possible involvement of DAP12, which forms a complex with TREM2, is not excluded; however, we and others observed lack of changes in *Tyrobp* mRNA in *Trem2*$^{-/-}$ brains (Wang et al., 2015) (Figure S5B). These findings reveal TREM2 as a component of the innate immune system essential for regulating the correct balance of hippocampal synapses. In this respect, TREM2 adds to complement proteins, in particular C1q and C3, which control synaptic pruning in the postnatal retinogeniculate system (Schafer et al., 2012; Stevens et al., 2007) and to MHC class I proteins, which promote the elimination of inappropriate connections during retinal and retinogeniculate circuit refinement (Boulanger and Shatz, 2004). Our data thus further support the relevance of the cross-talk between nervous and immune systems for correct brain development.

The impairment in microglia-dependent synapse elimination is likely at the origin of the hypoconnectivity detected in *Trem2*$^{-/-}$ mice, as recently described for mice lacking the chemokine receptor Cx3cr1 (Zhan et al., 2014). Of note, the strongest connectivity differences in *Trem2*$^{-/-}$ mice were seen between retrosplenial cortices, subiculum, anterior cingulate, and CA1 hippocampal area. The latter area contains a higher number of microglia as compared to other hippocampal regions such as the CA3 region (Jinno et al., 2007). Furthermore, microglia in CA1 are selectively more prone to being activated compared to DG or CA3 microglia (Vinet et al., 2012). Not surprisingly, CA1 is the area where microglia were mostly affected in developing *Trem2*$^{-/-}$ mice. Although further mechanisms may be involved, our findings thus support the view that the process of microglia-mediated synaptic pruning is central to the shaping of brain connectivity.

Brain circuits formed in the context of neurodevelopmental disorders in the presence of dysfunctional synapse elimination display abnormal features, such as hyper- or hypoconnectivity (Bernardinelli et al., 2014). For example, connectivity defects of neocortical circuits occur in different mouse models of autism, including the fragile X mental retardation 1 (Fmr1) (–/y) mouse model for fragile X syndrome, which shows a hyperconnectivity phenotype of the primary visual cortex with other neocortical regions (Haberl et al., 2015), and the homozygous mice lacking Cntnap2, a neurexin superfamily member associated with autism, which exhibit reduced long-range functional connectivity in prefrontal and midline brain hubs (Liska et al., 2018). These findings are in line with the alterations in brain connectivity widely detected in ASD patients, with hypoconnectivity dominating particularly for corticocortical and interhemispheric functional connectivity (Di Martino et al., 2014).

Interestingly, human imaging studies have unveiled a possible association between long-range hypoconnectivity and social

competence (Schreiner et al., 2014). Consistently, *Trem2*$^{-/-}$ adult mice exhibit decreased sociability, which occurs in the presence of intact cognitive functions. *Trem2*$^{-/-}$ mice also display excessive self-grooming, accompanied by defects in marble burying and juvenile play, in the absence of relevant cognitive impairments. Of note, microglia deletion of the autophagy *Aatg7* gene, which results in defective synaptic pruning, has been found to result in abnormal social interaction and repetitive behaviors, in the presence of intact cognitive functions (Kim et al., 2017). These data, together with the increased dendritic spine density detected in post-mortem ASD brains (Tang et al., 2014), enforce the picture that defects in synaptic pruning, later resulting in circuit hypoconnectivity and behavioral defects, may be at the origin of neurodevelopmental diseases, with microglial TREM2 being central to this process.

Consistent with this view, our data indicate that a subset of idiopathic ASD patients display reductions in TREM2 protein expression and show an inverse correlation between TREM2 and the ADI-R score. This is particularly evident in subjects between 5 and 23 years old, which represents the developmental period coinciding with synapse pruning in humans. These results therefore demonstrate that microglial TREM2 reductions, disrupting synapse pruning, may contribute to ASD and possibly to other neurodevelopmental diseases characterized by brain connectivity defects.

It will be important to assess to what extent TREM2 reductions are causative of ASD phenotypes. Electrophysiological slice recordings indicated a significant increase in mEPSC frequency, accompanied by higher dendritic spine density and social defects in *Trem2* heterozygous mice (Figures S5C–S5E). Although additional tests may be necessary to provide a more comprehensive picture, these data indicate that even partial reductions in TREM2 protein expression are sufficient to induce synaptic and behavioral defects. Genetic studies will be necessary to demonstrate the direct association between TREM2 and neurodevelopmental diseases. For example, it will be interesting to investigate whether the risk conferred by TREM2 defects for neurodegenerative diseases (Yeh et al., 2016) might originate, at least in part, from dysfunctional neuronal networks as described in our study.

STAR★METHODS

Detailed methods are provided in the online version of this paper and include the following:

SUPPLEMENTAL INFORMATION

Supplemental Information includes five figures and four tables and can be found with this article online at https://doi.org/10.1016/j.immuni.2018.04.016.

ACKNOWLEDGMENTS

We thank F. Colombo (FACS facility, Humanitas Research Institute) for assistance with flow cytometry and E. Ghirardini and I. Spera for help in performing some experiments. Work in the lab is supported by Ministero della Salute GR-2011–02347377, Cariplo 2015–0594 and "AMANDA" CUP_B42F16000440005 from regione Lombardia to M. Matteoli, and Fondazione Vodafone (E.M. and M. Matteoli). M.F. is supported by the Ontario Mental Health Foundation. F.F. was supported by a Fondazione Umberto Veronesi fellowship; M.T. is supported by a Fondazione Giancarla Vollaro Fellowship. V.Z. is supported by ETH Career Seed Grant SEED-42 16-1 and by the SNSF AMBIZIONE PZ00P3_173984 / 1. M. Markicevic was supported by ETH Research Grant ETH-38 16-2. R.C.P. is supported by the Synapsis Foundation - Alzheimer Research Switzerland ARS.

AUTHOR CONTRIBUTIONS

Conceptualization, Investigation, Methodology, Validation, Formal Analysis, and Data Curation, F.F. and R.M.; Conceptualization, Investigation, Formal Analysis, Supervision, and Funding Acquisition, M. Matteoli; Writing –Original Draft and Visualization, F.F. and M. Matteoli; Investigation, Methodology, Data Curation, and Formal Analysis, R.C.P., I.C., M.E., and V.Z.; Methodology and Data Curation, A.C., C.S.-C., F.P., M.T., F.C., and M.G.; Resources, K.O., L.P., S.V., and M.F.; Methodology and Formal Analysis, B.M. and M. Markicevic; Writing – Review & Editing, M. Matteoli, F.F., R.M., R.C.P., L.R., L.P., K.O., M.F., E.M., and V.Z.

DECLARATION OF INTERESTS

The authors declare no competing interests.

Received: August 15, 2017
Revised: January 19, 2018
Accepted: April 13, 2018
Published: May 8, 2018

REFERENCES

Arganda-Carreras, I., Fernández-González, R., Muñoz-Barrutia, A., and Ortiz-De-Solorzano, C. (2010). 3D reconstruction of histological sections: application to mammary gland tissue. Microsc. Res. Tech. *73*, 1019–1029.

Atagi, Y., Liu, C.C., Painter, M.M., Chen, X.F., Verbeeck, C., Zheng, H., Li, X., Rademakers, R., Kang, S.S., Xu, H., et al. (2015). Apolipoprotein E is a ligand for triggering receptor expressed on myeloid cells 2 (TREM2). J. Biol. Chem. *290*, 26043–26050.

Banker, G.A., and Cowan, W.M. (1977). Rat hippocampal neurons in dispersed cell culture. Brain Res. *126*, 397–425.

Beaudoin, G.M., 3rd, Lee, S.H., Singh, D., Yuan, Y., Ng, Y.G., Reichardt, L.F., and Arikkath, J. (2012). Culturing pyramidal neurons from the early postnatal mouse hippocampus and cortex. Nat. Protoc. *7*, 1741–1754.

Beckmann, C.F., and Smith, S.M. (2004). Probabilistic independent component analysis for functional magnetic resonance imaging. IEEE Trans. Med. Imaging *23*, 137–152.

Bernardinelli, Y., Nikonenko, I., and Muller, D. (2014). Structural plasticity: mechanisms and contribution to developmental psychiatric disorders. Front. Neuroanat. *8*, 123.

Biesemann, C., Grønborg, M., Luquet, E., Wichert, S.P., Bernard, V., Bungers, S.R., Cooper, B., Varoqueaux, F., Li, L., Byrne, J.A., et al. (2014). Proteomic screening of glutamatergic mouse brain synaptosomes isolated by fluorescence activated sorting. EMBO J. *33*, 157–170.

Boulanger, L.M., and Shatz, C.J. (2004). Immune signalling in neural development, synaptic plasticity and disease. Nat. Rev. Neurosci. *5*, 521–531.

Braun, N., Sévigny, J., Robson, S.C., Enjyoji, K., Guckelberger, O., Hammer, K., Di Virgilio, F., and Zimmermann, H. (2000). Assignment of ecto-nucleoside triphosphate diphosphohydrolase-1/cd39 expression to microglia and vasculature of the brain. Eur. J. Neurosci. *12*, 4357–4366.

Butovsky, O., Jedrychowski, M.P., Moore, C.S., Cialic, R., Lanser, A.J., Gabriely, G., Koeglsperger, T., Dake, B., Wu, P.M., Doykan, C.E., et al. (2014). Identification of a unique TGF-β-dependent molecular and functional signature in microglia. Nat. Neurosci. *17*, 131–143.

Cady, J., Koval, E.D., Benitez, B.A., Zaidman, C., Jockel-Balsarotti, J., Allred, P., Baloh, R.H., Ravits, J., Simpson, E., Appel, S.H., et al. (2014). TREM2 variant p.R47H as a risk factor for sporadic amyotrophic lateral sclerosis. JAMA Neurol. *71*, 449–453.

Cantoni, C., Bollman, B., Licastro, D., Xie, M., Mikesell, R., Schmidt, R., Yuede, C.M., Galimberti, D., Olivecrona, G., Klein, R.S., et al. (2015). TREM2 regulates microglial cell activation in response to demyelination in vivo. Acta Neuropathol. *129*, 429–447.

Colonna, M. (2003). TREMs in the immune system and beyond. Nat. Rev. Immunol. *3*, 445–453.

Corradini, I., Donzelli, A., Antonucci, F., Welzl, H., Loos, M., Martucci, R., De Astis, S., Pattini, L., Inverardi, F., Wolfer, D., et al. (2014). Epileptiform activity and cognitive deficits in SNAP-25(+/-) mice are normalized by antiepileptic drugs. Cereb. Cortex *24*, 364–376.

Correale, C., Genua, M., Vetrano, S., Mazzini, E., Martinoli, C., Spinelli, A., Arena, V., Peyrin-Biroulet, L., Caprioli, F., Passini, N., et al. (2013). Bacterial sensor triggering receptor expressed on myeloid cells-2 regulates the mucosal inflammatory response. Gastroenterology *144*, 346–356.e3.

Daws, M.R., Sullam, P.M., Niemi, E.C., Chen, T.T., Tchao, N.K., and Seaman, W.E. (2003). Pattern recognition by TREM-2: binding of anionic ligands. J. Immunol. *171*, 594–599.

Deacon, R.M. (2006). Digging and marble burying in mice: simple methods for in vivo identification of biological impacts. Nat. Protoc. *1*, 122–124.

Deacon, R.M., and Rawlins, J.N. (2006). T-maze alternation in the rodent. Nat. Protoc. *1*, 7–12.

Di Martino, A., Yan, C.G., Li, Q., Denio, E., Castellanos, F.X., Alaerts, K., Anderson, J.S., Assaf, M., Bookheimer, S.Y., Dapretto, M., et al. (2014). The autism brain imaging data exchange: towards a large-scale evaluation of the intrinsic brain architecture in autism. Mol. Psychiatry *19*, 659–667.

Grandjean, J., Schroeter, A., Batata, I., and Rudin, M. (2014). Optimization of anesthesia protocol for resting-state fMRI in mice based on differential effects of anesthetics on functional connectivity patterns. Neuroimage *102*, 838–847.

Grandjean, J., Zerbi, V., Balsters, J.H., Wenderoth, N., and Rudin, M. (2017). Structural basis of large-scale functional connectivity in the mouse. J. Neurosci. *37*, 8092–8101.

Greco, B., Managò, F., Tucci, V., Kao, H.T., Valtorta, F., and Benfenati, F. (2013). Autism-related behavioral abnormalities in synapsin knockout mice. Behav. Brain Res. *251*, 65–74.

Guerreiro, R., Wojtas, A., Bras, J., Carrasquillo, M., Rogaeva, E., Majounie, E., Cruchaga, C., Sassi, C., Kauwe, J.S., Younkin, S., et al.; Alzheimer Genetic Analysis Group (2013). TREM2 variants in Alzheimer's disease. N. Engl. J. Med. *368*, 117–127.

Haberl, M.G., Zerbi, V., Veltien, A., Ginger, M., Heerschap, A., and Frick, A. (2015). Structural-functional connectivity deficits of neocortical circuits in the Fmr1 (-/y) mouse model of autism. Sci. Adv. *1*, e1500775.

Hamerman, J.A., Pottle, J., Ni, M., He, Y., Zhang, Z.Y., and Buckner, J.H. (2016). Negative regulation of TLR signaling in myeloid cells–implications for autoimmune diseases. Immunol. Rev. *269*, 212–227.

Harris, K.M., and Stevens, J.K. (1989). Dendritic spines of CA 1 pyramidal cells in the rat hippocampus: serial electron microscopy with reference to their biophysical characteristics. J. Neurosci. *9*, 2982–2997.

Hickman, S.E., Kingery, N.D., Ohsumi, T.K., Borowsky, M.L., Wang, L.C., Means, T.K., and El Khoury, J. (2013). The microglial sensome revealed by direct RNA sequencing. Nat. Neurosci. *16*, 1896–1905.

Hsieh, C.L., Koike, M., Spusta, S.C., Niemi, E.C., Yenari, M., Nakamura, M.C., and Seaman, W.E. (2009). A role for TREM2 ligands in the phagocytosis of apoptotic neuronal cells by microglia. J. Neurochem. *109*, 1144–1156.

Huttner, W.B., Schiebler, W., Greengard, P., and De Camilli, P. (1983). Synapsin I (protein I), a nerve terminal-specific phosphoprotein. III. Its association with synaptic vesicles studied in a highly purified synaptic vesicle preparation. J. Cell Biol. *96*, 1374–1388.

Jenkinson, M., Bannister, P., Brady, M., and Smith, S. (2002). Improved optimization for the robust and accurate linear registration and motion correction of brain images. Neuroimage *17*, 825–841.

Ji, K., Akgul, G., Wollmuth, L.P., and Tsirka, S.E. (2013). Microglia actively regulate the number of functional synapses. PLoS ONE *8*, e56293.

Jinno, S., Fleischer, F., Eckel, S., Schmidt, V., and Kosaka, T. (2007). Spatial arrangement of microglia in the mouse hippocampus: a stereological study in comparison with astrocytes. Glia *55*, 1334–1347.

Jonsson, T., Stefansson, H., Steinberg, S., Jonsdottir, I., Jonsson, P.V., Snaedal, J., Bjornsson, S., Huttenlocher, J., Levey, A.I., Lah, J.J., et al. (2013). Variant of TREM2 associated with the risk of Alzheimer's disease. N. Engl. J. Med. *368*, 107–116.

Keren-Shaul, H., Spinrad, A., Weiner, A., Matcovitch-Natan, O., Dvir-Szternfeld, R., Ulland, T.K., David, E., Baruch, K., Lara-Astaiso, D., Toth, B., et al. (2017). A unique microglia type associated with restricting development of Alzheimer's disease. Cell *169*, 1276–1290.e17.

Kettenmann, H., Kirchhoff, F., and Verkhratsky, A. (2013). Microglia: new roles for the synaptic stripper. Neuron *77*, 10–18.

Kiialainen, A., Hovanes, K., Paloneva, J., Kopra, O., and Peltonen, L. (2005). Dap12 and Trem2, molecules involved in innate immunity and neurodegeneration, are co-expressed in the CNS. Neurobiol. Dis. *18*, 314–322.

Kim, H., Lim, C.S., and Kaang, B.K. (2016). Neuronal mechanisms and circuits underlying repetitive behaviors in mouse models of autism spectrum disorder. Behav. Brain Funct. *12*, 3.

Kim, H.J., Cho, M.H., Shim, W.H., Kim, J.K., Jeon, E.Y., Kim, D.H., and Yoon, S.Y. (2017). Deficient autophagy in microglia impairs synaptic pruning and causes social behavioral defects. Mol. Psychiatry *22*, 1576–1584. Published online July 12, 2016.

Kleinberger, G., Brendel, M., Mracsko, E., Wefers, B., Groeneweg, L., Xiang, X., Focke, C., Deußing, M., Suárez-Calvet, M., Mazaheri, F., et al. (2017). The FTD-like syndrome causing TREM2 T66M mutation impairs microglia function, brain perfusion, and glucose metabolism. EMBO J. *36*, 1837–1853.

Kober, D.L., Alexander-Brett, J.M., Karch, C.M., Cruchaga, C., Colonna, M., Holtzman, M.J., and Brett, T.J. (2016). Neurodegenerative disease mutations in TREM2 reveal a functional surface and distinct loss-of-function mechanisms. eLife *5*.

Krasemann, S., Madore, C., Cialic, R., Baufeld, C., Calcagno, N., El Fatimy, R., Beckers, L., O'Loughlin, E., Xu, Y., Fanek, Z., et al. (2017). The TREM2-APOE pathway drives the transcriptional phenotype of dysfunctional microglia in neurodegenerative diseases. Immunity *47*, 566–581.e9.

Lee, J.K., and Tansey, M.G. (2013). Microglia isolation from adult mouse brain. Methods Mol. Biol. *1041*, 17–23.

Liska, A., Bertero, A., Gomolka, R., Sabbioni, M., Galbusera, A., Barsotti, N., Panzeri, S., Scattoni, M.L., Pasqualetti, M., and Gozzi, A. (2018). Homozygous loss of autism-risk gene CNTNAP2 results in reduced local

and long-range prefrontal functional connectivity. Cereb. Cortex *28*, 1141–1153.

Lord, C., Rutter, M., and Le Couteur, A. (1994). Autism diagnostic interview-revised: a revised version of a diagnostic interview for caregivers of individuals with possible pervasive developmental disorders. J. Autism Dev. Disord. *24*, 659–685.

Lui, H., Zhang, J., Makinson, S.R., Cahill, M.K., Kelley, K.W., Huang, H.Y., Shang, Y., Oldham, M.C., Martens, L.H., Gao, F., et al. (2016). Progranulin deficiency promotes circuit-specific synaptic pruning by microglia via complement activation. Cell *165*, 921–935.

Mazaheri, F., Snaidero, N., Kleinberger, G., Madore, C., Daria, A., Werner, G., Krasemann, S., Capell, A., Trümbach, D., Wurst, W., et al. (2017). TREM2 deficiency impairs chemotaxis and microglial responses to neuronal injury. EMBO Rep. *18*, 1186–1198.

Menna, E., Zambetti, S., Morini, R., Donzelli, A., Disanza, A., Calvigioni, D., Braida, D., Nicolini, C., Orlando, M., Fossati, G., et al. (2013). Eps8 controls dendritic spine density and synaptic plasticity through its actin-capping activity. EMBO J. *32*, 1730–1744.

Miyamoto, A., Wake, H., Ishikawa, A.W., Eto, K., Shibata, K., Murakoshi, H., Koizumi, S., Moorhouse, A.J., Yoshimura, Y., and Nabekura, J. (2016). Microglia contact induces synapse formation in developing somatosensory cortex. Nat. Commun. *7*, 12540.

N'Diaye, E.N., Branda, C.S., Branda, S.S., Nevarez, L., Colonna, M., Lowell, C., Hamerman, J.A., and Seaman, W.E. (2009). TREM-2 (triggering receptor expressed on myeloid cells 2) is a phagocytic receptor for bacteria. J. Cell Biol. *184*, 215–223.

Neumann, H., and Takahashi, K. (2007). Essential role of the microglial triggering receptor expressed on myeloid cells-2 (TREM2) for central nervous tissue immune homeostasis. J. Neuroimmunol. *184*, 92–99.

Nicolini, C., Ahn, Y., Michalski, B., Rho, J.M., and Fahnestock, M. (2015). Decreased mTOR signaling pathway in human idiopathic autism and in rats exposed to valproic acid. Acta Neuropathol. Commun. *3*, 3.

Paloneva, J., Manninen, T., Christman, G., Hovanes, K., Mandelin, J., Adolfsson, R., Bianchin, M., Bird, T., Miranda, R., Salmaggi, A., et al. (2002). Mutations in two genes encoding different subunits of a receptor signaling complex result in an identical disease phenotype. Am. J. Hum. Genet. *71*, 656–662.

Paolicelli, R.C., Bolasco, G., Pagani, F., Maggi, L., Scianni, M., Panzanelli, P., Giustetto, M., Ferreira, T.A., Guiducci, E., Dumas, L., et al. (2011). Synaptic pruning by microglia is necessary for normal brain development. Science *333*, 1456–1458.

Parkhurst, C.N., Yang, G., Ninan, I., Savas, J.N., Yates, J.R., 3rd, Lafaille, J.J., Hempstead, B.L., Littman, D.R., and Gan, W.B. (2013). Microglia promote learning-dependent synapse formation through brain-derived neurotrophic factor. Cell *155*, 1596–1609.

Patel, A.X., Kundu, P., Rubinov, M., Jones, P.S., Vértes, P.E., Ersche, K.D., Suckling, J., and Bullmore, E.T. (2014). A wavelet method for modeling and despiking motion artifacts from resting-state fMRI time series. Neuroimage *95*, 287–304.

Peng, Q., Malhotra, S., Torchia, J.A., Kerr, W.G., Coggeshall, K.M., and Humphrey, M.B. (2010). TREM2- and DAP12-dependent activation of PI3K requires DAP10 and is inhibited by SHIP1. Sci. Signal. *3*, ra38.

Penzes, P., Cahill, M.E., Jones, K.A., VanLeeuwen, J.E., and Woolfrey, K.M. (2011). Dendritic spine pathology in neuropsychiatric disorders. Nat. Neurosci. *14*, 285–293.

Poliani, P.L., Wang, Y., Fontana, E., Robinette, M.L., Yamanishi, Y., Gilfillan, S., and Colonna, M. (2015). TREM2 sustains microglial expansion during aging and response to demyelination. J. Clin. Invest. *125*, 2161–2170.

Ransohoff, R.M., and Cardona, A.E. (2010). The myeloid cells of the central nervous system parenchyma. Nature *468*, 253–262.

Rayaprolu, S., Mullen, B., Baker, M., Lynch, T., Finger, E., Seeley, W.W., Hatanpaa, K.J., Lomen-Hoerth, C., Kertesz, A., Bigio, E.H., et al. (2013). TREM2 in neurodegeneration: evidence for association of the p.R47H variant with frontotemporal dementia and Parkinson's disease. Mol. Neurodegener. *8*, 19.

Riccomagno, M.M., and Kolodkin, A.L. (2015). Sculpting neural circuits by axon and dendrite pruning. Annu. Rev. Cell Dev. Biol. *31*, 779–805.

Schafer, D.P., Lehrman, E.K., Kautzman, A.G., Koyama, R., Mardinly, A.R., Yamasaki, R., Ransohoff, R.M., Greenberg, M.E., Barres, B.A., and Stevens, B. (2012). Microglia sculpt postnatal neural circuits in an activity and complement-dependent manner. Neuron *74*, 691–705.

Schafer, D.P., Lehrman, E.K., Heller, C.T., and Stevens, B. (2014). An engulfment assay: a protocol to assess interactions between CNS phagocytes and neurons. J. Vis. Exp. *88*, 51482.

Schmid, C.D., Sautkulis, L.N., Danielson, P.E., Cooper, J., Hasel, K.W., Hilbush, B.S., Sutcliffe, J.G., and Carson, M.J. (2002). Heterogeneous expression of the triggering receptor expressed on myeloid cells-2 on adult murine microglia. J. Neurochem. *83*, 1309–1320.

Schreiner, M.J., Karlsgodt, K.H., Uddin, L.Q., Chow, C., Congdon, E., Jalbrzikowski, M., and Bearden, C.E. (2014). Default mode network connectivity and reciprocal social behavior in 22q11.2 deletion syndrome. Soc. Cogn. Affect. Neurosci. *9*, 1261–1267.

Sethi, S.S., Zerbi, V., Wenderoth, N., Fornito, A., and Fulcher, B.D. (2017). Structural connectome topology relates to regional BOLD signal dynamics in the mouse brain. Chaos *27*, 047405.

Silverman, J.L., Tolu, S.S., Barkan, C.L., and Crawley, J.N. (2010). Repetitive self-grooming behavior in the BTBR mouse model of autism is blocked by the mGluR5 antagonist MPEP. Neuropsychopharmacology *35*, 976–989.

Stevens, B., Allen, N.J., Vazquez, L.E., Howell, G.R., Christopherson, K.S., Nouri, N., Micheva, K.D., Mehalow, A.K., Huberman, A.D., Stafford, B., et al. (2007). The classical complement cascade mediates CNS synapse elimination. Cell *131*, 1164–1178.

Stiles, J., and Jernigan, T.L. (2010). The basics of brain development. Neuropsychol. Rev. *20*, 327–348.

Takahashi, K., Rochford, C.D., and Neumann, H. (2005). Clearance of apoptotic neurons without inflammation by microglial triggering receptor expressed on myeloid cells-2. J. Exp. Med. *201*, 647–657.

Tang, G., Gudsnuk, K., Kuo, S.H., Cotrina, M.L., Rosoklija, G., Sosunov, A., Sonders, M.S., Kanter, E., Castagna, C., Yamamoto, A., et al. (2014). Loss of mTOR-dependent macroautophagy causes autistic-like synaptic pruning deficits. Neuron *83*, 1131–1143.

Tremblay, M.E., Lowery, R.L., and Majewska, A.K. (2010). Microglial interactions with synapses are modulated by visual experience. PLoS Biol. *8*, e1000527.

Turnbull, I.R., Gilfillan, S., Cella, M., Aoshi, T., Miller, M., Piccio, L., Hernandez, M., and Colonna, M. (2006). Cutting edge: TREM-2 attenuates macrophage activation. J. Immunol. *177*, 3520–3524.

Ulrich, J.D., Finn, M.B., Wang, Y., Shen, A., Mahan, T.E., Jiang, H., Stewart, F.R., Piccio, L., Colonna, M., and Holtzman, D.M. (2014). Altered microglial response to Aβ plaques in APPPS1-21 mice heterozygous for TREM2. Mol. Neurodegener. *9*, 20.

Vinet, J., Weering, H.R., Heinrich, A., Kälin, R.E., Wegner, A., Brouwer, N., Heppner, F.L., Rooijen, Nv., Boddeke, H.W., and Biber, K. (2012). Neuroprotective function for ramified microglia in hippocampal excitotoxicity. J. Neuroinflammation *9*, 27.

Wang, Y., Cella, M., Mallinson, K., Ulrich, J.D., Young, K.L., Robinette, M.L., Gilfillan, S., Krishnan, G.M., Sudhakar, S., Zinselmeyer, B.H., et al. (2015). TREM2 lipid sensing sustains the microglial response in an Alzheimer's disease model. Cell *160*, 1061–1071.

Wunderlich, P., Glebov, K., Kemmerling, N., Tien, N.T., Neumann, H., and Walter, J. (2013). Sequential proteolytic processing of the triggering receptor expressed on myeloid cells-2 (TREM2) protein by ectodomain shedding and γ-secretase-dependent intramembranous cleavage. J. Biol. Chem. *288*, 33027–33036.

Yeh, F.L., Wang, Y., Tom, I., Gonzalez, L.C., and Sheng, M. (2016). TREM2 Binds to apolipoproteins, including APOE and CLU/APOJ, and thereby facilitates uptake of amyloid-beta by microglia. Neuron *91*, 328–340.

Yeh, F.L., Hansen, D.V., and Sheng, M. (2017). TREM2, microglia, and neurodegenerative diseases. Trends Mol. Med. *23*, 512–533.

Yuan, P., Condello, C., Keene, C.D., Wang, Y., Bird, T.D., Paul, S.M., Luo, W., Colonna, M., Baddeley, D., and Grutzendler, J. (2016). TREM2 haplodeficiency in mice and humans impairs the microglia barrier function leading to decreased amyloid compaction and severe axonal dystrophy. Neuron *92*, 252–264.

Zalesky, A., Fornito, A., and Bullmore, E.T. (2010). Network-based statistic: identifying differences in brain networks. Neuroimage *53*, 1197–1207.

Zerbi, V., Grandjean, J., Rudin, M., and Wenderoth, N. (2015). Mapping the mouse brain with rs-fMRI: An optimized pipeline for functional network identification. Neuroimage *123*, 11–21.

Zhan, Y., Paolicelli, R.C., Sforazzini, F., Weinhard, L., Bolasco, G., Pagani, F., Vyssotski, A.L., Bifone, A., Gozzi, A., Ragozzino, D., and Gross, C.T. (2014). Deficient neuron-microglia signaling results in impaired functional brain connectivity and social behavior. Nat. Neurosci. *17*, 400–406.

Zhang, D., Snyder, A.Z., Shimony, J.S., Fox, M.D., and Raichle, M.E. (2010). Noninvasive functional and structural connectivity mapping of the human thalamocortical system. Cereb. Cortex *20*, 1187–1194.

Zwiers, M.P. (2010). Patching cardiac and head motion artefacts in diffusion-weighted images. Neuroimage *53*, 565–575.

STAR★METHODS

KEY RESOURCES TABLE

REAGENT or RESOURCE	SOURCE	IDENTIFIER
Antibodies		
Anti-Iba-1 Polyclonal Antibody, Unconjugated	Wako	Cat# 019-19741 RRID:AB_839504
Anti-Post Synaptic Density Protein 95, clone 6G6-1C9 antibody	Merck Millipore	Cat# MAB1596, RRID:AB_2092365
Guinea pig Anti-VGLUT 1 Polyclonal Antibody, Unconjugated	Synaptic Systems	Cat# 135 304, RRID:AB_887878
Anti-NeuN, clone A60 antibody	Millipore	Cat# MAB377, RRID:AB_2298772
Sheep Anti-Mouse Trem-2 Polyclonal antibody, Unconjugated	R and D Systems	Cat# AF1729, RRID:AB_354956
Purified anti-mouse CD68 antibody	BioLegend	Cat# 137001, RRID:AB_2044003
Rabbit Anti-Mouse P2Y12 Polyclonal Antibody, Unconjugated	AnaSpec; EGT Group	Cat# 55043A, RRID:AB_2298886
Rat Anti-Mouse CD68 Monoclonal antibody, Unconjugated, Clone FA-11	Bio-Rad / AbD Serotec	Cat# MCA1957T, RRID:AB_2074849
PSD-95 MAGUK scaffolding protein antibody (clone k28/43)	UC Davis/NIH NeuroMab Facility	Cat# 75-028, RRID:AB_2307331
Anti-GAPDH antibody	Synaptic Systems	Cat# 247 002, RRID:AB_10804053
Anti-Shank2 antibody	Synaptic Systems	Cat# 162 202, RRID:AB_2619860
Anti-beta3 Tubulin Monoclonal Antibody, Unconjugated	Promega	Cat# G7121, RRID:AB_430874
Anti-SV2 A antibody	Synaptic Systems	Cat# 119 002, RRID:AB_887802
Goat Anti-Human Trem-2 Polyclonal antibody, Unconjugated	R and D Systems	Cat# AF1828, RRID:AB_2208689
Mouse Anti-beta-Actin Monoclonal Antibody, Unconjugated, Clone AC-74	Sigma-Aldrich	Cat# A2228, RRID:AB_476697
Goat anti-Mouse IgG (H+L) Secondary Antibody, Alexa Fluor 555 conjugate	Thermo Fisher Scientific	Cat# A-21422, RRID:AB_2535844
Goat anti-Rabbit IgG (H+L) Secondary Antibody, Alexa Fluor 488 conjugate	Thermo Fisher Scientific	Cat# A-11034, RRID:AB_2576217
Goat anti-Rabbit IgG (H+L) Highly Cross-Adsorbed Secondary Antibody, Alexa Fluor 555	Thermo Fisher Scientific	Cat# A-21429, RRID:AB_2535850
Goat anti-Rat IgG (H+L) Cross-Adsorbed Secondary Antibody, Alexa Fluor 555	Thermo Fisher Scientific	Cat# A-21434, RRID:AB_2535855
Goat anti-Guinea Pig IgG (H+L) Highly Cross-Adsorbed Secondary Antibody, Alexa Fluor 488	Thermo Fisher Scientific	Cat# A-11073, RRID:AB_2534117
Donkey anti-Sheep IgG (H+L) Cross-Adsorbed Secondary Antibody, Alexa Fluor 633	Thermo Fisher Scientific	Cat# A-21100, RRID:AB_2535754
Donkey Anti-Mouse IgG, IRDye 680 Conjugated antibody	LI-COR Biosciences	Cat# 926-32222, RRID:AB_621844
Goat Anti-Mouse IgG, IRDye 680 Conjugated antibody	LI-COR Biosciences	Cat# 926-32220, RRID:AB_621840
MAP2ab (Microtubule-associated protein 2 ab) antibody	Immunological Sciences	Cat# MAB-10334, RRID:AB_2314767
APC/Cy7 anti-mouse/human CD11b antibody	BioLegend	Cat# 101226, RRID:AB_830642)
PerCP anti-mouse CD45 antibody	BioLegend	Cat# 103130, RRID:AB_893339
MHC Class II (I-A/I-E) Monoclonal Antibody (M5/114.15.2), PE, eBioscience(TM)	Thermo Fisher Scientific	Cat# 12-5321-83, RRID:AB_465929
Alexa Fluor 488 anti-mouse CD86 antibody	BioLegend	Cat# 105018, RRID:AB_493462
Alexa Fluor 647 anti-mouse CX3CR1 antibody	BioLegend	Cat# 149004, RRID:AB_2564273
CD80 (B7-1) Monoclonal Antibody (16-10A1), APC, eBioscience(TM)	Thermo Fisher Scientific	Cat# 17-0801-82, RRID:AB_469417
CD39 Monoclonal Antibody (24DMS1), PE-Cyanine7, eBioscience(TM)	Thermo Fisher Scientific	Cat# 25-0391-82, RRID:AB_1210766
FM1-43FX dye	Thermo Fisher	Cat#F35355

(*Continued on next page*)

Continued

REAGENT or RESOURCE	SOURCE	IDENTIFIER
Biological Samples		
Human brain tissue samples	Autism BrainNet, Simons Foundation Autism Research Initiative	http://autismbrainnet.org/about-us/portal/
Chemicals, Peptides, and Recombinant Proteins		
Hoechst 33342	Thermofisher	Cat# H3570
B27 supplement	Thermofisher	CAT#17504044
Lipofectamine 2000	Thermofisher	Cat#11668019
Neurobasal medium	Gibco	Cat#21103-049
okadaic acid	Sigma	Cat#08010
Triton X-100	Roche	Cat#11332481001
Carestream Kodak Processing chemicals Kodak Fixer	Sigma	Cat#P6567
DAPI	Biolegend	Cat#: 422801
Fluorsave	Calbiochem	Cat#345789
Tetrodotoxin	Tocris	Cat#1078
D-AP5	Tocris	Cat#0106
(-)-Bicuculline methiodide	Tocris	Cat#2503
Critical Commercial Assays		
Live/Dead Fixable dead cell stain kits	Molecular Probes	L34955
NucleoSpin RNA extraction kit	Machery Nagel	Cat#740955.10
RNeasy MICRO KIT	QIAGEN	Cat#74004
High-capacity cDNA Reverse Transcription Kit	Applied Biosystems	Cat#4368814
ECL Prime Western Blotting Detection Reagent	Sigma	Cat#GERPN2232
Experimental Models: Organisms/Strains		
Mouse: C57BL/6 (CD45.2)	Harlan	C57BL/6 RRID: IMSR_JAX000664
Mouse: *Trem2*$^{-/-}$	Turnbull et al., 2006	N/A
Oligonucleotides		
Rn18S (Mm03928990_g1)	Thermofisher	Cat#4331182
Tnf (Mm00443258_m1)	Thermofisher	Cat#4331182
Tyrobp (Mm00449152_m1)	Thermofisher	Cat#4331182
Tgfb1 (Mm01178820_m1)	ThermoFisher	Cat#4331182
Il1b (Mm0043228_m1)	Thermofisher	Cat#4331182
Aif1 (Mm00479862_g1)	Thermofisher	Cat#4331182
P2ry12 (Mm01950543_s1)	Thermofisher	Cat#4331182
Software and Algorithms		
ImageJ	NIH software	https://imagej.nih.gov/ij/; RRID:SCR_003070
IMARIS software (3D microglia reconstruction)	Bitplane	RRID: SCR:_007370
GraphPad Prism 6	GraphPad Software	RRID: SCR:_002798
FlowJo 8.7	TreeStar; FlowJo	RRID: SCR:_008520
pClamp-10 software	(Axon Instruments, Foster City, CA)	https://www.moleculardevices.com; RRID:SCR_011323
Image Lab software	Bio-Rad	http://www.bio-rad.com/en-us/sku/1709690-image-lab-software?ID=1709690; RRID:SCR_014210

CONTACT FOR REAGENT AND RESOURCE SHARING

Further information and requests for resources and reagents should be directed to and will be fulfilled by the Lead Contact, Michela Matteoli (michela.matteoli@hunimed.it).

EXPERIMENTAL MODEL AND SUBJECT DETAILS

Mouse Strains

Mice were housed in the SPF animal facility of Humanitas Clinical and Research Center in individually ventilated cages. All experiments followed the guidelines established by the European Directive 2010/63/EU and the Italian D.Lg. 26/2014. The study was approved by the Italian Ministry of Health. All efforts were made to minimize the number of subjects used and their suffering. C57BL/6 *Trem2*$^{-/-}$ mice, generated as previously described (Turnbull et al., 2006) were provided by Bioxell-Cosmo Pharmaceutical (Milan, Italy) (Correale et al., 2013). P18-20 and P90 male and female animals were used for each experiment, except for behavioral analysis where only male mice were used. All the experiments were performed on littermates. Littermates and non-littermates were used for behavioral experiments (except for the sociability test where only non-littermates were tested). Immunohistochemistry results were also confirmed in brain slices obtained from the Trem2$^{-/-}$ mouse line maintained at Washington University School of Medicine and provided by L.P. *Trem2*$^{-/-}$ and littermate control WT mice (backcrossed 12 generations to the C57BL/6 background) were obtained from Marco Colonna (Turnbull et al., 2006) and the two strains were bred in parallel.

Human brain tissue samples

Frozen post-mortem fusiform gyrus samples from subjects with idiopathic autism (n=16) and controls (n=17) were provided by "Autism BrainNet, a resource of the Simons Foundation Autism Research Initiative now including also the Autism Speaks' Autism Tissue Program (see Tables S1 and S2: Characteristics of Control samples (S1) and ASD samples (S2)).

Tissue samples were stored at −80°C before use. Clinical information on the samples was obtained through the Autism Tissue Program online portal (http://autismbrainnet.org/about-us/portal/). The diagnosis of autism was confirmed using the Autism Diagnostic Interview-Revised *post-mortem* through interviews with the parents and/or caregivers (see Table S4). Samples from subjects with known genetic causes of autism spectrum and related disorders (Rett, Asperger etc.) were excluded. There were no significant differences between groups for age and *post-mortem* interval (two-tailed Student's t-test p=0.359 and p=0.686, respectively).

Primary cell culture

Neuronal cultures

Mouse hippocampal neurons were established from the hippocampi of embryonic stage E17 fetal mice or from postnatal 1-2 day-old pups as described previously (Banker and Cowan, 1977; Beaudoin et al., 2012) with slight modifications. Neurons were plated onto glass coverslips coated with poly-L-lysine at densities of 95 cells/mm^2. The cells were maintained in Neurobasal medium (Invitrogen) with B27 supplement and antibiotics, 2 mM glutamine and glutamate. All experiments were performed at 13-15 days *in vitro* (DIV).

Microglial cultures

Primary microglia were obtained from mixed cultures prepared from the hippocampi and cerebral cortices of mice at postnatal day (P)1-5. Microglial cells were isolated by shaking flasks for 45 min at 230 rpm at day 10 after plating. Cells were then seeded on poly-L-ornithine (Sigma) pre-coated wells at a density of 1.5×10^5 cell/mL in DMEM containing 20% heat-inactivated fetal bovine serum (FBS). For microglia to neuron co-culture experiments, WT or *Trem2*$^{-/-}$ microglia were added to hippocampal neurons (13-14 DIV) at a microglia to neuron ratio of 1.5:1 for 24 hr. In a distinct set of experiments, microglia were plated in transwell culture inserts (0.4 μm pore, Costar) - at the same microglia to neuron ratio as above, - to prevent contact with neurons. To visualize neuronal processes and dendritic spines, hippocampal neurons were transfected using Lipofectamine 2000 at DIV11.

METHOD DETAILS

Assessment of cell viability

The viability of WT and *Trem2*$^{-/-}$ microglia was assessed by incubating the cells for 15 min at 37°C with Hoechst 33342 (2 μg/ml) and Propidium Iodide (PI) (1 μg/ml). The staining was assessed using an Olympus IX53 Inverted Microscope. Cells were counted in four microscopic fields per each well (four biological replicates per WT and *Trem2*$^{-/-}$ microglia) and expressed as the percentage of PI positive cells per the total number of Hoechst positive cells. The analysis was performed by using ImageJ NIH software.

Brain microglia isolation and Flow Cytometry

Isolation of adult microglia was adapted from (Lee and Tansey, 2013). Briefly, anesthetized mice at P18-P20 were perfused intracardially with ice-cold Hank's balanced salt solution (HBSS), and the hippocampi and cortices were dissected. The different areas were mechanically homogenized and digested in digestion buffer (DMEM/F12 containing 1 mg/ml Papain, 1.2 U/ml Dispase II, 20 U/ml DNAse I (Sigma) and 0.7 U/ml Collagenase D (Roche) at 37 °C for 30 min, washed and centrifuged 5 min at 250g. Homogenates were filtered through a 40 μm cell strainer (Becton Dickinson, Heidelberg, Germany). Hippocampal cells were resuspended in PBS + 2% FBS, counted and kept on ice until staining for FACS analysis. Pellets from cortices were resuspended in 4 ml of 37% Percoll (Sigma) and added to a 15ml conical tube containing 4 ml of 70% Percoll. 4 ml of 30% Percoll and 2 ml of HBSS were added to the top of the gradient. The gradient was centrifuged at 300g for 40 min. Microglial cells were collected from the 37%/70% interphase, and total cell counts were determined. Isolated microglia from hippocampi and cortices were labeled with a combination of conjugated antibodies (see above), and FACS analysis of the microglial profile was performed by gating CD11b$^+$CD45^{low} cells. Appropriate antibody IgG isotype controls were used for all staining. FACS analysis was performed on a FACS Canto II machine

(BD Biosciences), and data were analyzed with FlowJo Software (TreeStar). To sort microglial cells from the different brain areas, a Becton Dickinson FACSARIA III cell sorter was used.

RNA isolation and RT-qPCR

Total RNA was extracted using a NucleoSpin RNA extraction kit according to the manufacturer's protocol. RNA from sorted microglia was amplified and extracted by an RNeasy MICRO KIT. Total RNA (20-40ng) was used in 20-40 μl of reverse transcription reaction (high-capacity cDNA Reverse Transcription Kit). The ΔΔCt method was applied to determine differences in gene expression levels after normalization to the arithmetic mean of GAPDH or 18S rRNA or of the microglial genes *AIF-1* and *P2yr12* as an internal standard. The TaqMan probes were the following: Rn18S; Aif1; P2ry12; Tnf; *Tyrobp*; *Tgfb1*; *Il1b*. All data are mean of duplicates, and the standard errors of the mean were calculated between duplicates or triplicates. Real-time PCR was performed using ViiA7 (Applied Biosystems).

In vitro engulfment assay

Phagocytosis assay of apoptotic neurons

Neurons were cultured for 10-14 DIV and okadaic acid (30 nM) was added for 3hr to induce apoptosis. Apoptotic neurons were detached, collected and then labeled with CFSE (spell out). After labeling, apoptotic neuronal membranes were washed three times and added to WT or *Trem2*$^{-/-}$ microglial cultures at a microglia/neuron ratio of 1:20 for 24hr. Microglia were next enzymatically detached with accutase (Millipore), stained with CD11b antibody and analyzed by FACS.

Phagocytosis of beads

Fluorescent particles (3μm) (Spherotech) were added to microglial cells at a 1:1 or 1:2 microglia/beads ratio for 2hr. Cells were washed with ice-cold PBS, enzymatically detached with accutase, stained with CD11b antibody and analyzed by FACS as described above.

Synaptosome purification and engulfment assay

Synaptosomes were purified as previously described (Huttner et al., 1983) and conjugated with FM 1-43FX dye in HBSS at 4°C for 2 min (modified from (Biesemann et al., 2014)). Unbound FM 1-43FX dye was washed out with multiple rounds of centrifugation. WT or *Trem2*$^{-/-}$ microglia, plated at a density of 1.5×10^5 cell/mL, were then incubated with 5 μl of FM 1-43FX dye-conjugated synaptosomes for 2 and 24 hr. Microglia were next enzymatically detached and analyzed by FACS.

Immunocytochemistry and cell imaging

Cells were fixed for 10-15 min at room temperature (RT) in 4% (w/v) PFA, 4% (w/v) sucrose, 20 mM NaOH and 5 mM MgCl2 in PBS, pH 7.4. For intracellular staining, cells were permeabilized and blocked for 30–60 min at RT in 15% (w/v) goat serum, 0.3% (v/v) Triton X-100, 450 mM NaCl, 20 mM phosphate buffer, pH 7.4 and incubated at 4 °C overnight with primary antibodies diluted in blocking buffer. Confocal images were acquired with a laser scanning confocal microscope Olympus Fluo View FV1000, using a UPL S APO 60x/1.35 oil objective (Olympus), and with a LEICA SP8 STED3X confocal microscope, using a HC PL APO 100x/1.40 oil white objective (Leica). Emission filter bandwidths and sequential scanning acquisition were set up in order to avoid any possible spectral overlap between fluorophores. Deconvolution was applied to images shown in Figures 3C and 3F using Huygens Professional software (SVI, Scientific Volume Imaging). Images were finally processed with Fiji and Imaris 7.4.2 software (Bitplane).

Dendritic spine analysis

Images of primary hippocampal cultures were acquired using a UPL S APO 60x/1.35 oil objective (Olympus). Each image consisted of a stack of images taken through the z-plane of the GFP-transfected hippocampal neurons. Spine analysis was performed with ImageJ. On the basis of morphology, spines were classified into the following categories: 1) Filopodia: spines with a long neck and a visible small head; 2) Mushroom: big spines with a well-defined neck and a very voluminous head (Harris and Stevens, 1989). At least four dendritic branches were analyzed for each neuron. The number of analyzed neurons is reported in each figure legend. At least three independent replications were performed for each experimental setting.

Immunohistochemistry

Mice were anesthetized with a ketamine (100 mg kg−1)/xylazine (20 mg kg−1) cocktail and perfused with 0.9% saline, followed by 4% paraformaldehyde. Immunofluorescent staining was carried out on free-floating 50 μm-thick sections. Sections at the level of the dorsal hippocampus were processed by 45 min RT blocking in 10% Normal Goat serum 0.2% Triton X-100 and overnight incubation with specific primary antibodies Iba-1 (1:1000); PSD95 (1:200, Millipore); VGLUT1 (1:1000); NeuN (1:1000); Trem2 (1:400; R&D System); CD68 (1:1000; Biolegend); P2Y12 (1:1000) followed by incubation with secondary antibodies (1:400, Alexa Fluor®-conjugated, Invitrogen), counterstained with DAPI and mounted in Fluorsave (Calbiochem). For TREM2 and P2Y12 staining, slices were permeabilized at RT in 0.5% Triton X-100 (Sigma), followed by 1 hr RT blocking in 2% BSA 0.5% Triton X-100 and overnight incubation with primary antibody. Z-stack confocal images were acquired with a laser scanning confocal microscope Olympus Fluo View FV1000, using a UPLFLN 40x/1.30 or a UPLSAPO 60x/1.35 oil objective (Olympus). Images were acquired in the *pyramidal layer* or *stratum radiatum* of the CA1 subfield of the hippocampus, as indicated. For microglial counts and morphologic analysis, confocal images for the selected marker Iba-1 were modified as 8-bit and Z-stack projection images. Iba-1 and DAPI$^+$ cells were counted per HPF. The resulting images were smooth processed, binarized and skeletonized, using the Skeletonize Plugin for ImageJ (Arganda-Carreras et al., 2010). Before quantification, a mask using the particle analysis function was created to subtract from skeletonized images. The resulting images were

processed by choosing the Analyze Skeleton 2D 3D option in the Skeletonize Plugin, and the number of branches and junctions per cell were obtained from the Results tables.

In vivo synapse engulfment quantification

Fixed brain slices from WT and *Trem2*$^{-/-}$ littermates were permeabilized for 45 min at RT in 0.5% Triton X-100, followed by 1 hr RT blocking in 2% BSA 0.5% Triton X-100 and overnight incubation with primary antibody for PSD-95 (1:100, Millipore), CD68 (1:400, Bio-Rad) and Iba-1 (1:600, Wako) at 4°C. Upon washing, sections were incubated 2 hr at RT with Alexa-fluorophore-conjugated secondary antibodies (1:400, Invitrogen). Confocal microscopy was performed with a TCS-SP8 (Leica) Laser Scanning System, by using a Leica HCX PL APO 63X/ NA 1.3, glycerol-immersion lens. Images were acquired with 3X digital zoom, as 61.5μmX61.5μm in XY, and with z-step size of 0.33μm. Stacks ranged from 5 to 6μm in thickness. Images were processed and analyzed by Imaris Software (Bitplane, Switzerland). CD68 and Iba-1 volumes were quantified by applying 3D surface rendering of confocal stacks in their respective channels, using identical settings (fix thresholds of intensity and voxel) within each experiment. Each confocal acquisition contained an equal number of WT and Knockout images. For quantification of PSD95 engulfment by microglia, only PSD95 puncta present within microglial CD68^{+} structures were considered. This procedure was used to ensure that only puncta entirely phagocytosed by microglia were included in the analysis. To this aim, a new channel for ''engulfed PSD95'' was created, by using the mask function in Imaris, masking the PSD95 signal within CD68^{+} structures. Quantification of volumes for 'engulfed PSD95 in CD68' was performed following the '3D Surface rendering of engulfed material' protocol, previously published by (Schafer et al., 2014). To account for variations in cell size, the amount of 'engulfed PSD95 in CD68' was normalized to the total volume of the phagocyte (given by Iba-1^{+} total volume). Total PSD95 volume per field from the same confocal stacks was also quantified following the same protocol. All the data were normalized to WT values within each experiment.

Golgi staining

Mice (P18-P20 and P90) were anesthetized and perfused intracardially as described above (immunohistochemistry section). The brains were removed and stained by a modified Golgi-Cox method as described in (Menna et al., 2013), with slight modifications. Coronal sections of 100 μm thickness from the dorsal hippocampus were obtained using a vibratome (VT1000S, Leica, Wetzlar, Germany). These sections were collected free floating in 6% sucrose solution and processed with ammonium hydroxide for 13 min, followed by 7 min in Kodak Film Fixer, and finally were rinsed with distilled water, placed on coverslips, dehydrated and mounted with a xylene-based medium. Spine density was counted on the secondary branches of apical dendrites of pyramidal neurons located in the CA1 subfield of the dorsal hippocampus. At least 30 neurons per animal were evaluated.

Nissl staining

Brains were perfused as described above, and consecutive 50 μm-thick coronal sections (200 μm apart) were mounted on charged-coated slides, rehydrated, stained with cresyl violet dye (Sigma), and mounted on coverslips with DPX (spell out) (Thermo Scientific). The thickness of the pyramidal layer of the CA1 region of the hippocampus was measured using ImageJ. Five different measurements were performed along the pyramidal layer for each image.

Electrophysiology

Slice recordings

To obtain acute hippocampal slices, *Trem2*$^{-/-}$, *Trem2*$^{+/-}$ and WT mice aged 18-20 days were deeply anesthetized as previously described and decapitated. Brains were removed and placed in ice-cold solution containing the following (in millimolar): 87 NaCl, 21 NaHCO3, 1.25 NaH2PO4, 7 MgCl2, 0.5 CaCl2, 2.5 KCl, 25 D-glucose, and 7 sucrose, equilibrated with 95% O2 and 5% CO2 (pH 7.4). Coronal slices (300 μm thick) were cut with a VT1000S vibratome from the hippocampus. Slices were incubated at RT for at least 1 hr, in the same solution as above, before being transferred to the recording chamber. During experiments, slices were perfused at 2.0 mL/min with artificial cerebrospinal fluid (ACSF) containing the following (in millimolar): 135 NaCl, 21 NaHCO3, 0.6 CaCl2, 3 KCl, 1.25 NaH2PO4, 1.8 MgSO4, and 10 D-glucose, aerated with 95% O2 and 5% CO2 (pH 7.4). Cells were examined with a BX51WI upright microscope (Olympus) equipped with a water immersion differential interference contrast (DIC) objective and an infrared (IR) camera (XM10r Olympus).

Neurons were voltage (or current) clamped with a Multiclamp 700B patch-clamp amplifier (Molecular Devices, Union City, CA) at RT. Low-resistance micropipettes (2–3 MΩ) were pulled from borosilicate glass. The cell capacitance and series resistance were always compensated. Experiments in which series resistance did not remain below 10 MΩ (typically 5-8 MΩ) were discarded. Input resistance was generally close to 100-200 MΩ. Synaptic currents were low-pass filtered at 2 kHz, sampled at 10kHz and analyzed with pClamp/Digidata 1440A (Molecular Devices). Recordings were made from hippocampal CA1 or CA3 pyramidal neurons. For miniature excitatory post-synaptic current (mEPSC) recordings, 1 μM TTX, 20μM Bicuculline and 50μM AP5 were added to the ACSF. Pipettes contained (in millimolar): 135 K^{+}-gluconate, 1 EGTA, 10 HEPES, 2 $MgCl_2$, 4 MgATP, and 0.3 Tris-GTP, (pH 7.4).

Cell culture recordings

Whole cell voltage-clamp recordings were performed on WT and transgenic embryonic or postnatal hippocampal neurons maintained in culture for 13-15 DIV. During recordings, cells were bathed in a standard external solution containing (in mM): 125 NaCl, 5 KCl, 1.2 MgSO4, 1.2 KH2PO4, 2 CaCl2, 6 glucose, and 25 HEPES-NaOH, pH 7.4. Recording pipettes (resistances of 3-5 MΩ) were filled with a standard intracellular solution containing (in mM): 135 K^{+}-gluconate, 1 EGTA, 10 HEPES, 2 $MgCl_2$, 4 MgATP,

and 0.3 Tris-GTP, (pH 7.4). For mEPSC recordings, 1μM tetrodotoxin, 20μM Bicuculline and 50μM AP5 were added to the standard extracellular solution to block spontaneous action potential propagation by GABA-A and NMDA receptors. Recordings were performed in voltage clamp mode at a holding potential of -70 mV using a Multiclamp 700B amplifier and pClamp-10 software (Axon Instruments, Foster City, CA). Series resistance ranged from 10 to 20 MΩ and was monitored for consistency during recordings. Cells in culture with leak currents >100 pA were excluded from the analysis. Signals were amplified, sampled at 10 kHz, filtered to 2 or 3 KHz, and analyzed using the pClamp 10 data acquisition and analysis program.

Magnetic resonance imaging

10 *Trem2*$^{-/-}$ mice (6/4 m/f) and 10 wildtype littermates (6/4 m/f) underwent MRI scanning. There were no significant bodyweight differences between the genotypes, however, there was a significant effect of sex on bodyweight in both groups (p-value<0.001). MRI scanning was performed to evaluate brain functional and structural changes in comparison to their respective wildtype littermates. The levels of anesthesia and mouse physiological parameters were monitored following an established protocol to obtain a reliable measurement of functional connectivity (Zerbi et al., 2015) (Grandjean et al., 2014). Briefly, anesthesia was induced with 4% isoflurane and the animals were endotracheally intubated and the tail vein cannulated. Mice were positioned on a MRI-compatible cradle and artificially ventilated at 80 breaths per minute, 1:4 O2 to air ratio, and 1.8 ml/h flow (CWE, Ardmore, USA). A bolus injection of medetomidine 0.04 mg/kg and pancuronium bromide 0.1 mg/kg was administered, and isoflurane was reduced to 1%. After 5 min, an infusion of medetomidine 0.09 mg/kg/h and pancuronium bromide 0.2 mg/kg/h was administered, and isoflurane was further reduced to 0.5%. Animal temperature was monitored using a rectal thermometer probe, and maintained at 36.5 °C ± 0.5 during the measurements with a water heating system in the cradle. The preparation of the animals did not exceed 10 minutes.

Data acquisition was performed on a Biospec 70/16 small animal MR system (Bruker BioSpin MRI, Ettlingen, Germany) equipped with a cryogenic quadrature surface coil (Bruker BioSpin AG, Fällanden, Switzerland). To capture blood oxygenation dependent (BOLD) images, we used a standard gradient-echo echo planar imaging sequence (GE-EPI, repetition time TR = 1 s, echo time TE = 15 ms, in-plane resolution RES = 0.22 × 0.2 mm2, number of slice NS = 20, slice thickness ST = 0.4 mm, slice gap SG = 0.1 mm, 900 volumes). In addition, we acquired diffusion weighted images for white matter structural integrity evaluation (DWI, multi-shot SE-EPI sequence, 4 segments, TR = 2 s, TE = 22 ms, RES = 0.2 × 0.2 mm2, NS = 28, ST = 0.4 mm, SG = 0 mm, b-values = 0-1000 s/mm2, 94 directions encoding, for a total scan time of 9 min).

Data pre-processing and statistics

Rs-fMRI

Resting state fMRI datasets were preprocessed using an existing pipeline for removal of unwanted confounds from the time-series (Zerbi et al., 2015), with modifications (Sethi et al., 2017). Rs-fMRI examines the temporal correlations of slow fluctuations of the blood oxygen level dependent (BOLD) signal across the brain during rest, i.e., without overt perceptual inputs or motor output typically present in traditional fMRI studies. The coherence of BOLD fluctuations between brain regions (i.e., functional connectivity) is a parameter often used to determine the brain's capability to share and integrate information (Zhang et al., 2010) and can be used as translational tool to study complex circuitry interactions and their pathology in laboratory animals (Grandjean et al., 2017; Haberl et al., 2015; Zerbi et al., 2015). Briefly, each rs-fMRI dataset was fed into MELODIC (Multivariate Exploratory Linear Optimized Decomposition of Independent Components) (Beckmann and Smith, 2004) to perform a within-subject spatial-ICA with a fixed dimensionality estimation (number of components set to 100). This included correction for head motion using MCFLIRT (Jenkinson et al., 2002) and in-plane smoothing with a 0.3 × 0.3 mm kernel. We applied FSL-FIX with a study-specific classifier obtained from an independent dataset of 15 mice and used a 'conservative' removal of the variance of the artifactual components. Thereafter, FIX-cleaned datasets were despiked (Patel et al., 2014), band-pass filtered (0.01-0.25 Hz), coregistered to the skull-stripped T2-weighted images and normalized to the AMBMC template (http://imaging.org.au/AMBMC/AMBMC) using ANTs v2.1 (http://picsl.upenn.edu/software/ants/).

Diffusion tensor parameter estimation

Through measurement of water diffusivity in multiple directions, diffusion tensor MRI reconstructs an ellipsoid to model the diffusion in every voxel. The pre-processing steps consisted of individual realignment of the diffusion images, followed by eddy current correction and tensor estimation. Briefly, the diffusion tensor was estimated for every voxel using the PATCH algorithm (Zwiers, 2010). This method incorporates motion correction and is robust against both regional artifacts (e.g. cardiac motion) and slice-wise artifacts (e.g. bulk motion) by providing a weight for every voxel that reflects the probability of being an outlier in the tensor fitting. From the eigenvalues of the diffusion tensor, fractional anisotropy (FA) maps were calculated. The resulting volumes were spatially normalized to the AMBMC template using linear affine and non-linear elastic transformations in ANTs.

Behavioral analysis

Marble burying

Marble burying was assessed as previously described (Deacon, 2006). Digging and marble burying in mice: simple methods for in vivo identification of biological impacts. Briefly, each mouse was placed individually into a clean mouse cage with 4 cm deep bedding and 12 glass marbles were placed in a regular pattern on the surface. The number of marbles that were buried by each mouse in 30 min was measured.

Self-grooming

Mice were scored for spontaneous grooming behaviors as described earlier (Silverman et al., 2010) with slight modifications. Each mouse was placed individually into a clean mouse cage with a thin (0.5 cm) layer of bedding reducing neophobia, while preventing digging, a potentially competing behavior. After 5 minutes acclimatization, each mouse was scored with a stopwatch for 10 min for cumulative time spent grooming all body regions by an expert observer.

Nestlet shredding

Each mouse was placed individually into a cage containing a single, preweighed nestlet and left undisturbed in the cage with the nestlet for 30 min. After returning the mouse to its home cage, the remaining intact nestlet material was removed from the cage with forceps and allowed to dry overnight. The day after, the remaining unshredded nestlet material was weighted and the weight was divided by the starting weight to calculate the ratio of intact nestlet material.

Sociability and social recognition

Sociability and social novelty tasks were performed as previously described (Corradini et al., 2014). The apparatus consists of a 3-compartment transparent polycarbonate box (20x40x22(h) cm each), with two sliding doors (5x8(h)cm), opening on the central compartment, that can be closed to confine the animal. The proband mouse was habituated in the central compartment for 5 min. For sociability assessment, an unfamiliar adult C57Bl/6 male mouse was placed in one side compartment whereas the opposite contained an empty wire cage. Immediately after the sociability task, the social novelty test was carried out in the same apparatus without any cleaning, placing a new unfamiliar mouse in the wire cage that had been empty during the prior 10-min session. Familiar and unfamiliar animals from different home cages had never been in physical contact with the subject mice or with each other. For both tests, the time spent in each chamber was recorded for 10 min.

Juvenile play interaction

Social interaction was tested between pairs of unfamiliar mice. Each pair of mice was placed into the test cage (a standard mouse cage with a thin layer of bedding) for the 10-min test session. Test sessions were recorded and scored at a later time by an expert observer, and the time spent sniffing each other was recorded.

Water maze place navigation

Spatial memory was assessed in a Morris water maze as previously described (Corradini et al., 2014) with minor modification. Briefly, mice were trained and tested in a circular pool arena made of white polypropylene (diameter 100 cm, wall height 60 cm), filled with water (made opaque by the addition of paint) to a height of 30 cm and maintained at 24–26°C. A 10-cm diameter target platform of transparent polypropylene was placed 0.5 cm below the water surface in the N, S, E, or W quadrant at 15 cm from the wall. Each mouse was released into the pool from different starting points and was trained for a constant platform position over three days with six trials per day separated by 30–60 min intervals and each trial lasting maximally 120 s. After this acquisition phase, mice were subjected to reversal training lasting for 2 days with the platform positioned in the opposite quadrant. The latency to find the escape platform was measured.

Spontaneous alternation

The T-maze was constructed of gray plexiglass, with a stem length of 40 cm and arm length of 90 cm; each section was 11 cm wide with 19 cm high side walls. Each mouse was placed at the maze start and was allowed to enter either arm. After being confined to the chosen arm for 30 seconds, each animal was removed and replaced in the start area for a new trial. Each mouse was subjected to 8 trials, each trial lasting maximally 60 seconds. The percentage of alternation was calculated (Deacon and Rawlins, 2006). Animals showing freezing behavior, who did not move in the maze, were excluded from the analysis.

Open field

General motor activity was tested in an open field task in P20 and P90 mice. Mice were placed in a multi-unit open field maze (MED Associates) with field chamber (25 cm long and 25 cm wide), and activity was recorded using Activity Monitor software (MED Associates). Each chamber was digitally divided into four zones using the Activity Monitor software. Data were collected continually for 30 min and the distance traveled (cm), ambulatory counts, zone entries, resting time, time spent in the corners or close to the walls, and average velocity were all recorded and scored automatically.

Western blots

Mouse tissues

Hippocampi and cortices were homogenized in 62.5 mM Tris pH 8, 290 mM sucrose, 1% sodium dodecyl sulfate (SDS) supplemented with protease inhibitors (Roche). The total protein concentration of each sample was determined by BCA (Thermo Fisher), and equal amounts of total protein (15μg) were loaded onto 12% Tris–HCl gels (Bio-Rad). Following electrophoresis, proteins were transferred to a 0.45 μM nitrocellulose membrane (Bio-Rad). Blots were probed overnight at 4 °C with primary antibodies (anti-PSD95 (1:10.000, NeuroMab); anti-GAPDH (1:1000); anti-Shank2 (1:2000); anti-SV2 (1:1000); anti-actin (1:10.000); anti-β3 tubulin (1:5000); anti-MAP2 (1:1000)) and next incubated with HRP-conjugated secondary antibodies at 1:5000 for 2 hr at room temperature. ECL Prime Western Blotting Detection Reagent (GE Healthcare) was used for detection of the signal. Visualization and imaging of blots was performed by means of Chemi-Doc system and Image Lab software (Bio-Rad). All the Western blotting were run twice.

Human tissues

Protein extraction for Western blot analysis was performed as previously described (Menna et al., 2013; Nicolini et al., 2015). For each sample, 70 μg of total protein was resolved on a 12% SDS-polyacrylamide gel. Samples were resolved on 4 gels, each containing a standard curve consisting of 5, 20, 50 and 90 μg of total protein from a control human cortex sample. After transfer, the membranes

(Immobilon-FL; Millipore, Etobicoke, Ontario, Canada) were probed overnight at 4°C with primary antibodies to TREM2 (1:1000, R&D Systems), β-actin (1:2000) and GAPDH (1:500 R&D). Primary and secondary antibodies (1:10000) were diluted in Odyssey Blocking Buffer (LI-COR Biosciences) mixed with phosphate-buffered saline containing 0.05% Tween-20 at a ratio of 1:1 for primary antibodies and 1:4 for secondary antibodies. Signals were detected and quantified using an Odyssey Imaging System (LI-COR Biosciences).

QUANTIFICATION AND STATISTICAL ANALYSIS

Data are displayed as individual dots and mean ± SEM, except for Figures 1L, 3G–3I, 4C, 4D, 5D, S1A–S1D, S1G, S2A–S2C, S2F, S5B, and S5D where the data are presented as bar graph with mean ± SEM. For each graph, the number of observations indicated with "n" and the number of biological replicates (mice) indicated with "N" can be found in the figure legends. Differences between multiple groups were analyzed by one-way ANOVA with a Bonferroni's or Tukey's or Dunn's post hoc test. Comparisons between two groups following a normal distribution were analyzed using an unpaired t-test (two-tail distribution) or a Mann-Whitney test as indicated in each figure. Statistical analysis was performed using GraphPad Prism (Graph-Pad Software). Differences were considered to be significant if $p \leq 0.05$ and are indicated by *; those at $p \leq 0.01$ are indicated by **; those at $p \leq 0.001$ are indicated by ***; those at $p \leq 0.0001$ by ****.